Electrochimica Acta 461 (2023) 142600

Contents lists available at ScienceDirect

Electrochimica Acta

journal homepage: www.journals.elsevier.com/electrochimica-acta

Phosphate ions detection by using an electrochemical sensor based on laser-scribed graphene oxide on paper

Bernardo Patella [a,1,*], Antonino Parisi [a,1], Nadia Moukri [a], Federico Gitto [a,c], Alessandro Busacca [a], Giuseppe Aiello [a], Michele Russo [b], Alan O'Riordan [c], Rosalinda Inguanta [a]

[a] Dipartimento di Ingegneria, Università degli Studi di Palermo, Italy
[b] Dipietro Group, Siracusa, Italy
[c] Nanotechnology group, Tyndall National Institute, University College Cork, Dyke Prade, Cork, Ireland

ARTICLE INFO

Keywords:
Phosphate ions
Electrochemical sensor
Voltammetry
Reduced graphene oxide
Paper-based sensors
Laser scribed

ABSTRACT

In this work, electrodes based on laser-scribed reduced graphene oxide were fabricated using filter paper as the substrate. To fabricate the electrodes, a water suspension of graphene oxide was filtered to produce a continuous and uniform film of graphene oxide on the filter paper surface. Subsequently, a CO_2 laser was used to "write" the working, counter and reference eelctroes by reducing graphene oxide in specific areas to define complete sensors. Referecnce electrodes were then coated with a commercial Ag/AgCl conductive paste to produce a quasi Ag/AgCl reference. As fabricated devices were employed as electrochemical sensors for detection of phosphate ions in water by employing the molybdenum blue method. This method exploits the reaction between molybdate and phosphate ions in acidic media leading to a Keggin-type complex ($PMo_{12}O_{40}^{3-}$) which, being electrochemically active, enables the indiret detection of phosphate ions. Sensors exhibited high selectivity and sensitive detection of phosphate ions in a wide linear range, from 1 to 20 μM; with a limit of detection of 0.4 μM. To demonstrate that sensors could be utilized for *in-situ* phosphate ion detection, paper substrate was first pre-loaded with sulphuric acid and molybdate ions. During analysis, these chemicals were then desorbed directly into the test sample eliminating the need for any kind of external manipulation or reagent addition. Thus, this paper presents the fabrication of a portable, easy-to-use, biodegradable and fast phosphate ions sensor for in situ and real-time monitoring of water quality.

1. Introduction

In recent years, the monitoring and quantification of water contamination is a topic of great interest [1,2]. Pollutants are released, on a daily basis, into underground and drinking waters creating a hazard for water ecosystems, health and the environment [3,4]. The most common inorganic contaminants present in underground and drinking waters are nitrates, nitrite, phosphate, sulfate, chloride, fluoride, lead, copper, mercury, arsenic and cadmium [5–11]. These species are harmful not only to the environment but also to human health. Consequently, for their effective non-laboratory based monitioring, it is very important to develop new and innovative techniques that are not only capable of analyzing water in real-time and in situ but are also economically viable, fast and easy to use [12]. The current methods to quantify these species are typically ICP-MS (Inductively coupled plasma mass spectrometry), HPLC (High-performance liquid chromatography), and titrimetry, among others [13,14]. Unfortunately, these techniques are laboratory based and require highly trained personnel and consequently do not fit with the requirements for a fast and point-of-use analysis of water . In contrast, electrochemical sensors are very suitable for point-of-use sensig as analyte quantification is based on its oxidation/reduction at the electrode/electrolyte interface [15]. This oxidation/reduction may occur at very low applied potentials, and thus can be carried out with very low power consumption and can be powered using a small commercial battery. Furthermore, depending on test analyte(s) properties, the appropriate electrochemical technique can be selected, from a range of different techniques, making the approach very versatile [16–21]. Several electrochemical sensors for water monitoring, such as for antibiotics, nitrates, chloride, mercury, and silver have been reported int eh literature [22–34]. The performance of electrochemical sensors can be further improved by using nanostructured electrodes to create a very high electrochemically active surface area with low

* Corresponding author.
[1] These authors contributed equally to this work.

https://doi.org/10.1016/j.electacta.2023.142600
Received 19 January 2023; Received in revised form 29 April 2023; Accepted 15 May 2023
Available online 18 May 2023

overpotential for redox reactions [35–40]. Finally, electroanalysis may be applied to non-electroactive species as it is possible to use indirect methods of analysis [24,41–43]. This approach may be applied to phosphate ions as they cannot be easily directly detected using traditional electrochemical sensors [44].

The main source of water contamination from phosphate arises from agricultural activities through the improper use of phosphorus-based fertilizers [45,46]. The excess of phosphate ions leads to water eutrophication causing the proliferation of algal blooms. These blooms are very dangerous for aquatic life through the consumption of dissolved oxygen in water and also blocking and preveting sunlight from reaching the underwater plants [47,48]. In addition, high concentrations of phosphate in water limits microbial growth damaging the whole aquatic ecosystem through a loss of bio-diversity [49]. For these reasons, the United States Environmental Protection Agency (US-EPA) has set specific limits for phosphate concentrations in different water bodies. Specifically, phosphate cannot exceed 100 ppb in water not diverted to reservoirs, 50 ppb in effluents discharging into reservoirs, and no more than 25 ppb in water within reservoirs [50]. These limits are unfortunately often exceeded as demonstrated by the Irish EPA who monitors the phosphate concentration in rivers and lakes. They found that 26% of rivers had a concentration higher than 35 ppb, while for lakes the concentration was higher than 25 ppb; with an average increase of 2% over the last 5 years [51]. In 2016, 7.7% of Irish groundwater exceeded the limit of 35 ppb of phosphate set by the water frame work directive [51].

The quantification of phosphate in human body fluids is another area of interest as it is related to various diseases [52]. For example, in the case of hyperphosphatemia (elevated levels of phosphate in blood) kidney damage, bone and teeth fragility can occur [53]. Nowadays, the main method to quantify phosphate is based on a spectrophotochemical technique. In particular, the sample containing phosphate ions is treated with acid and molybdate salts to produce the Keggin ion, named phospho-molybdenum blue, as follows:

$$7PO_4^{3-} + 12Mo_7O_{24}^{6-} + 72H^+ \Leftrightarrow 7PMo_{12}O_{40}^{3-} + 36H_2O \quad (1)$$

This reaction occurs only at extremely low pH (ranging from 0 to 2), hence the need requirement to add acid to the sample. Following the reaction, the absorbance in the blue region of of the spectrum is measured(using colorimetry) and correlated with PO_4^{3-} ion concentration [54,55]. Unfortunatley the colorimetric method has a low sensitivity and is subject to errors related to the refractive index and turbidity of the sample [24]. However, the formation of the Keggin ion can also be exploited by electrochemical sensor as this species can be electrochemically reduced as follows:

$$PMo_{12}O_{40}^{3-} + nH^+ + ne^- \Leftrightarrow H_nPMo_{12}O_{40}^{3-} \quad (2)$$

|Multiple reports are present in the literature that use this indirect electrochemical method [44,52,56–61]. The main disadvantage of this procedure is the need to treat the water sample by adding strong acid and molybdate ions. This requriement significantly limits the application of this approach to in-situ and real-time water analysis. However, this disadvantage can be overcome by impregnating the sensor substrate with the required reagents as demonstrated by Cinti et al. [62]. In particular, they developed a reagent-free paper-based sensor using a wax printer and a screen-printing technique. Their sensor enabled the quantification of phosphate ions in a wide linear range, up to 300 μM, with a detection limit of 4 μM.

Concerning the active sensor material, graphene-based electrodes are widely used in electroanlaysis [56,63]. Graphene-based materials have excellent properties, such as high surface area, aspect ratio, porosity, electrical conductivity and mechanical stability [64,65]. Among the graphene-based materials, graphene oxide (GO) is particularly interesting [66,67] as GO forms stable solutions in water due to the presence of different oxygen-based functional groups (oxyl, hydroxyl, carboxyl) [68,69]. Unlike graphene, it is an insulating material but it becomes conductive when is converted into its reduced form (reduced graphene oxide, rGO) [70]. rGO can be produced using different reduction methods (thermally, chemically or electrochemically) leading to different degree of reduction, so a mixture of rGO and GO is almost always obtained [71–74]. An interesting technique to produce rGO is the use of a CO_2 laser beam. The excitation of C═O bonds is strong enough to break them (releasing O_2) and thus reduces GO in localized and precise areas [75–77]. Moreover, the same laser can also be used to partially (or completely cut) parts of the substrate to produce, in a single step, the standard three-electrode configuration required for electrochemical sensors [23]. The process is very easy to carry out, is cheap and can be applied for mass manufacture of rGO-based electrodes, as demonstrated by Liu et al. [78]. The degree of reduction can be controlled by optimizing the operating conditions such as laser beam power, dwell time and the number of passes by the laser [77,79]. This method has been used to fabricate sensors for monitoring of pH [80,81], biomolecules [82–85], bacteria [86], virus [87], proteins [88], cortisol [89], dopamine [90], insecticides [91], glucose [80,92,92], ammonia [93], urea [94], heavy metals [95] and hydrogen peroxide [96]. In these reports glass, ITO, polydimethylsiloxane, PET, polyimide and plastics were used as the substrate.

In this work, filter paper was employed as a asubstrate material and laser scribing employed to fabricaterGO-based sensors for phosphate ion quantification. To fabricate the sensor, an aquesous solution of GO was filtered using a Whatman filter paper to create a continuous film on the paper surface. The electrodes were then defined by direct writing, or scribing, using a a CO_2 laser operating under computer numerical control. Finally, sensors were laser cut from the paper substrate to produce the final sensor configuration. Specifically, working and counter electrodes consisted of as prepared laser-scribed reduced graphene oxide (LSrGO), while a Ag/AgCl paste was used to coat the reference area. To fabricate a ready-to-use device, the filter paper -based sensors were first impregnated with sulphuric acid and molybdate ions. During measurement, these species are released into the water sample that thus can be analyzed without the addition of any other reagents. The fabricated sensors were applied to PO_4^{3-} detection using the phospho-molybdenum blue method and demonstrated a limit of detection of 0.4 μM (35 ppb). River water samples were also analyzed and the results compared favourably with those obtained using standard colorimetric technique.

2. Experimental

2.1. Sensors fabrication and characterization

Silver and Ag/AgCl conductive pastes were purchased from Nanografi (Turkey, Ankara) while filter paper (FP) (Whatman®, grade 50) from Cytiva (United States,Marlborough), graphene oxide (4 mg/mL, >99%) from Graphenea (Spain, San Sebastian). All other reagents were purchased from Alpha Aesar (United States, Tewksbury). Filter paper was used as the substrate for sensor fabrication. Firstly one side of the paper was gold-sputtered using an Emitech K575X sputter coater (DUE EMME, Italy, Cormano) to render it conductive. The top of the paper was covered with a mask to avoid the shorcut of the electrodes. Then, an aqueous solution of GO (0.5 mg/mL) was filtered on the sputtered side using a vacuum laboratory setup. Different volumes (from 1 to 20 mL) of GO solution were used to optimize GO thickness. Following filtration, substrates were air dried for 3 h at 40 °C. To fabricate the sensor devices, the paper substrates were placed in a laser cutter equipped with a CO_2 laser beam (with a nominal power of 50 W) to seletively reduce GO in rGO (Maitech, MT-5030W50DSK, Italy, Vanzaghello). Using AutoLaser® software, three-electrode shapes with a gap of 1.5 mm between each electrode was scribed. The reference and working electrodes were rectangular in shape (10 mm long and 4.5 mm wide) whereas the counter electrode was 'L' shape (4.5 mm wide and 20 mm long). The

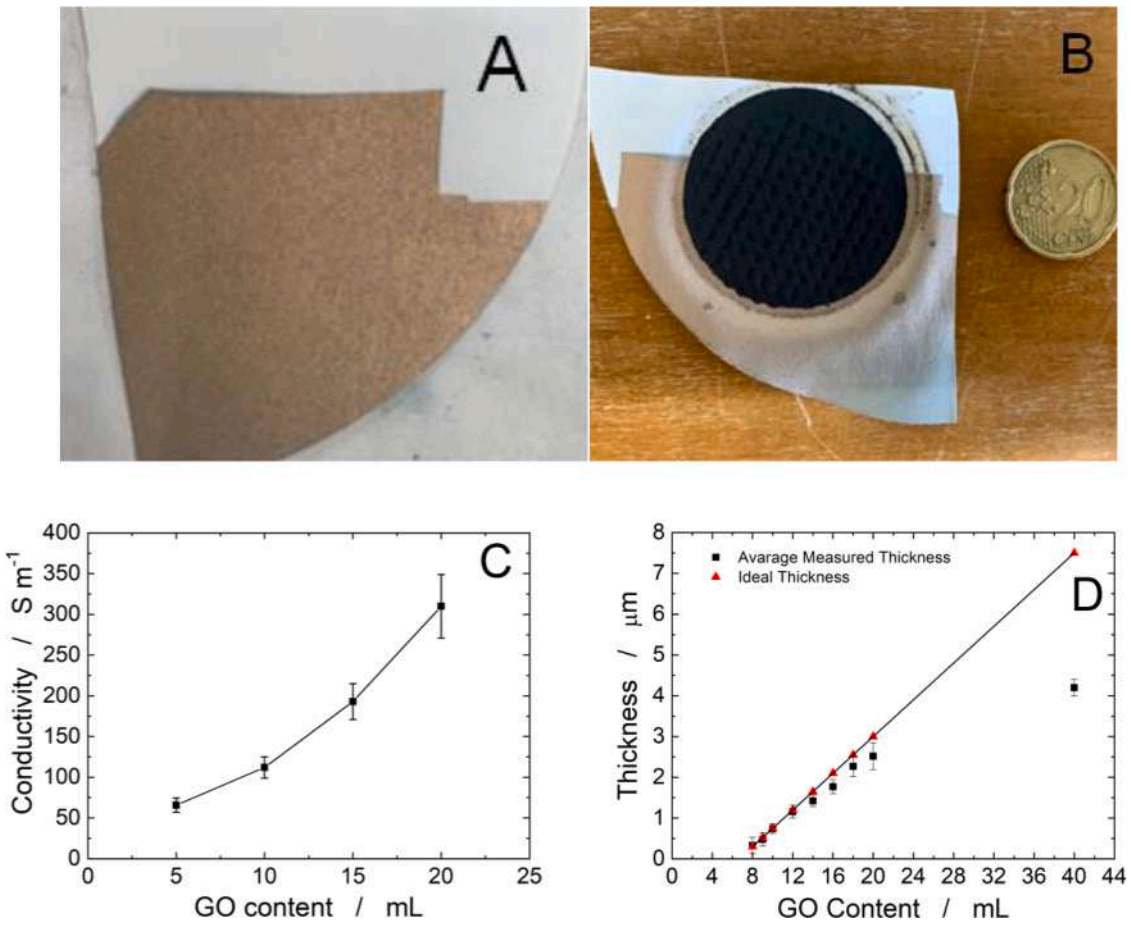

Fig. 1. Filter paper substrate after A) sputtering and B) filtration of 20 mL of 0.5 mg/mL of GO solution. Effect of GO content on C) the conductivity of the electrode and D) on the GO thickness.

laser power and the scan speed were chosen to provide both low electrical resistance and good mechanical stability. After laser scribing, the reference electrode was coated with Ag/AgCl paste while the external electrical contacts were made using a silver paste;both pastes were air-cured at 80 °C for 30 min in an oven.

To optimize laser speed and power, the sheet resistance of samples was measured using a four-point probe method with a source measure unit instrument (Keithley 2440, United States, Cleveland). The sheet resistance and resistivity were measured for both GO and rGO specimens at room temperature, respectively. GO was probed as a narrow strip with a length-to-width ratio of 10, to reduce the measurement error arising from to the geometry of the samples.To minimize contact resistance Ag-contact pads were created at both ends of the strip and a direct current four-point measurement method was used. The measurement current was limited to 0.1 mA to prevent self-heating of the samples under test. The sheet resistance of the samples was calculated by dividing the resistance measured by the number of squares in the strip. The resistivity of the samples was calculated by multiplying the sheet resistance by the thickness of the layer. Finally, sheet conductance and conductivity were obtained as the inverse of sheet resistance and resistivity, respectively [97,98]

Following fabrication, samples were characterized using scanning electron microscopy (SEM, FEG-ESEM, FEI QUANTA 200, United States, Waltham) and energy dispersive spectroscopy (EDS, AMETEK, United States, Berwyn). These characterization methods are presented in detail in [42,99,100].XRD was performed using a RIGAKU diffractometer (D-MAX 25,600 HK, Japan, Tokyo). All diffractograms were obtained in the 2θ range from 5° to 100° with a step of 0.02° and a measuring time of 0.5 s per step, using copper Kα radiation (λ= 1.54 Å), a tube voltage of 40 kV and a current of 30 mA. XPS was performed using a ULVAC-PHI PHI 5000 Versa Probe II Scanning XPS Microprobe™ (Japan, Osaka). This apparatus is equipped with an Al Kα (1486.6 eV) source in a FAT mode. The XPS spectra were collected with the 128 channels hemispherical analyzer at a pass energy of 23.5 eV and energy step size of 0.05 eV. Raman analysis was undertaken using a Renishaw inVia Raman Microscope (England, Gloucestershire) equipped with a He:Ne laser (633 nm) and calibrated using the Raman peak of polycrystalline Si (520 cm^{-1}). Diffraction patterns, Raman and XPS spectra were analysed by comparison with spectra in the published literature. Sensor thicknesses and average surface roughness were measured using a thickness gauge (ARW Surfix, Phynix, Italy, Zanè) and by a surface profilometer (Dektak 3030 stylus profilometer, United States, San Diego).

To eliminate the need to add reagents during analysis, substrates were immersed for different times in a solution containing both sulphuric acid and ammonium molybdate solutions. In this way, the paper substrates were impregnated with these reagents; which would then be released during the phosphate analysis. After immersion, sensors were dried at room temperature. To quantify the sorbed reagents, impregnated sensors were soaked in deionized water where sulphuric acid and ammonium molybdate were subsequently released. The water was then analyzed measuring its pH and molybdate concentration for the different immersion times. The solution pH was analyzed with a standard pH meter (Hanna HI 2211) whereas molybdate concentration was quantified with a colorimetric assaymeasured using an Infinite 200 PRO plate reader (Tecan Group Ltd., Switzerland). Specifically, a solution containing 50 mM of phosphate, 0.54 µM of tin and molybdate ranging from 0.05 to 0.5 mM was used. Then, the absorbance, at 740 nm, was measured and plotted against initial molybdate ion concentration to

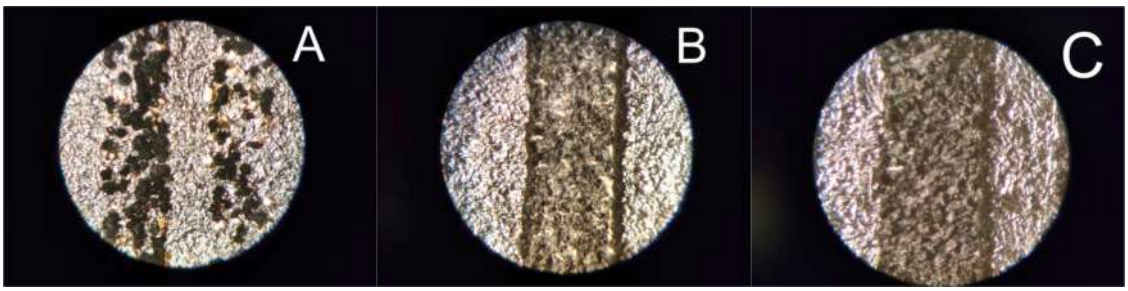

Fig. 2. Optical microscopy of the electrode surfaces reduced with a laser scanning speed of A) 25 mm/s, B) 200 mm/s and C) 75 mm/s at 1.85 W.

generate the calibration line. The impregnation time and the concentrations of molybdate and sulphuric acid were explored woth a a final solution with 100 μM of molybdate ions and a pH of 1.56 selected.

2.2. Sensor performance

As-prepared sensors were mounted in a 3D printed cell (acrylonitrile butadiene styrene, ABS) using a Zortrax printer (M200, Poland, Olsztyn). Electrochemical characterization was undertaken using a multichannel potentiostat (Solartron 1470E, United States, Gastonia). The exposed areas of the working and reference electrodes was 33 mm^2 each while for the counter electrode hadan area of 180 mm^2. Sensor was first electrochemically characterized by measuring the electrochemical active surface area (ECSA) by the double layer capacitance method [101]. Cyclic voltammetry (CV) was carried out from +200 to +400 mV vs Ag/AgCl electrode, in the non-faradaic region, at different scan rates, from 5 to 1000 mV/s. Both cathodic and anodic capacitive currents were recorded and the difference (Δj) at +300 mV was plotted against the scan rate (v). The ECSA was evaluated as the slope of the Δj vs scan rate plot.

Electrochemical quantification of phosphate ions was carried out in a 0.05 M H_2SO_4 aqueous solutions (pH = 1.56) using CV performed in the voltage range of −500 mV to +500 mV vs Ag/AgCl, with a scan rate of 25 mV/s. Different concentrations of phosphate ions (as orthophosphate acid) from 1 to 1000 μM were measured After baseline subtraction (using the 0 μM solution), the reduction peak current intensity (located at −100 mV) was used. Each experiment was carried out at least three times using a new electrode each time.

Phosphate sensor selectivity was studied by measuring 0.1 mM of phosphate in the presence of 1 mM of different possible interferent species (sodium, potassium, nitrate, nitrite, sulfate, lead, aluminum, zinc, iodide, silicate and copper). These interferents were selected as they are commonly present in river water samples.

To validate the sensor, the phosphate concentration of river water samples were also quantified using the standard colorimetric assay. River water samples (Oreto, Palermo) were collected and tested without any pretreatment.This was undertaken following the procedure proposed by Dickman et al. [102]. Specifically, standard solutions containing 3 μM of molybdate, 0.54 μM of tin with phosphate ranging from 1 to 20 μM were prepared and the absorbance at 740 nm was measured and plotted against PO_4^{3-} concentration. River water samples were then analyzed by adding the same concentrations of molybdate and tin to 160 μL of a sample.

3. Results and discussion

3.1. Sensor fabrication and optimization

The fabrication of LSrGO-based sensors is a multistep process that starts with sputtering a thin gold layer followed by the filtration of the GO solution on the sputtered side of the Whatman filter paper. Gold was sputtered on just 75% of the paper area to avoid electrical shorting of the three-electrode system using a mask. The final goal was to obtain a fully integrated sensor with counter, reference and working electrodes all on the same substrate. The three electrodes are electrically isolated from each other with the external contacts made in the unsputtered region of the substrate, as shown in Fig. 1A.. The GO filtration porecess was optimized to yield a uniform and crack-free continuous GO film since the presence of cracks will destroy the electrical conductivity of an electrode. However, it is noted that during the laser treatment and/or during sensor manipulation some formation of small cracks is almost inevitable. Following filtration, the filtrate appeared completely clear indicating that the filter paper was able to completely retain the GO on the paper surface.

Figure 1B shows a filter paper substrate after filtering 20 mL of GO (corresponding to 10 mg of GO) solution.The ideal conditions in terms of thickness, compactness, uniformity and stability of GO filmwere evaluated by measuring the electrical conductivity of the electrodes after laser reduction and evaluating the surface morphology by SEM. SEM ananlysis showed a compact and uniform film, which covered the entire surface of the substrate, was obtained only with solution volumes greater than 10 mL. For lower volumes, the film was not compact and also did not cover the entire surface. This means that, after the laser reduction, some parts of rGO easily detached from the substrate making it unusable.

The effect of GO content on the conductivity of the fabricated electrode was studied by first reducing the GO layer with a CO_2 laser beam using 1.875 W power and 75 mm/s and speed, respectively. As described in Fig. 1C, the conductivity of the electrodes increased with the increasing GO content due to an enhanced rGO thickness and uniformity. The error bars show good repeatability of the GO reduction process. The conductivity vs GO content shows a supralinear trend. This behavior is attributable to simultaneous variations in thickness and uniformity of the GO layer with increasing filtered volume. Small volumes led to the formation of an uneven and thin layer which, during the laser reduction, tended to form separate clods/islands of rGO and consequenlty lower conductivity. Higher volumes, on the other hand, lead to the formation of compact and uniform GO layers, which after laser reduction continue to be uniform and exhibit high conductivity. Furthermore, the greater the amount of GO on the filter, the higher the mechanical stability of the reduced GO however, the higher the amount of the GO on the filter paper the longer the filtration time whichincreased exponentially.

The thickness of the filtered GO layer was examined using a thickness gauge. Specifically, ten different points were measured for each sample and an average value calculated. As reported in [103], the vacuum filtration method enabled films with a controllable thickness to be produced. We found that the GO thickness increased linearly with increasing volume of the filtered GO solution (from 1 to 6 mL), see Fig. 1D. For larger volumes of filtered solution, the rate of GO thickness growth gradually decreased. As the volume of solution to be filtered increased, and therefore the GO content, the filtration process required more and more time. As the filtration takes place, the fibers of the filter paper supports were progressively covered with GO, reducing the flow

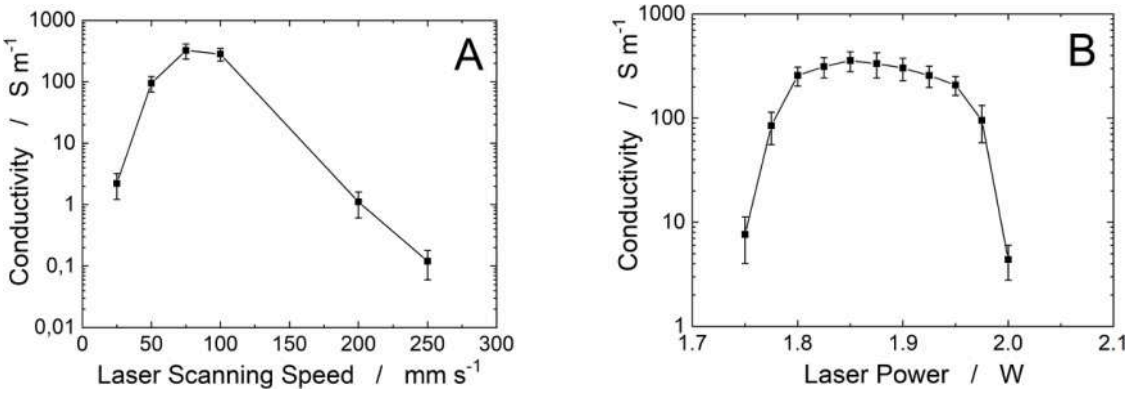

Fig. 3. Effect of A) laser scanning speed and B) laser power on rGO conductivity.

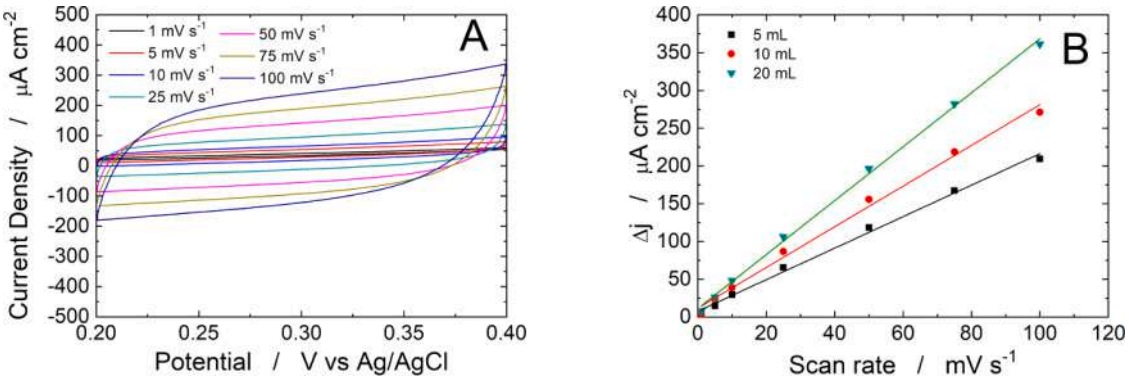

Fig. 4. A) CV curves obtained in PBS solution at different scan rates and B) corresponding plot of the Δj (difference of cathodic and anodic current at 0.3 V vs Ag/AgCl) vs scan rate.

of the permeate, especially during the final part of the process when a film is formed on the filter surface. Once filtration was complete, the vacuum was maintained to suck air through the filter paper to dry the film. This step together with the long filtration time led to the formation of compact GO films. Thus, 20 mL of GO was chosen as the best volume for the filtration process. Larger volumes were discounted to avoid excessively long filtration times. In addition, Fig. 1D shows that there would be very little gain in terms of thickness. The final thickness of the optimized GO layer was ~ 4.15 ± 0.15 µm.

The effect of laser power and scanning speed was studied to optimize the reduction process of the GO. Both parameters are very important and must be optimized to produce stable and reproducible rGOelectrodes [104]. Very low scanning speed lower than 25 mm/s cannot be used because both the GO layer and the paper substrate were burned (Fig. 2A). For scanning speeds up to 50 mm/s the paper substrate was stable but the GO layer was still slightly burned.

Very high scanning speeds, above 200 mm/s, produced a nonuniform layer of LSrGO which tended to a have a cloud type morphology characterized by a high electrical resistivity. Additionaly, at high scanning speeds the GO areas treated with the laser also exhibited poorly defined edges, Fig. 2B. The best results were observed in the scanning range from 50 to 100 mm/s (Fig. 2C). In this range, a maximum conductivity of about 300 S/m was found at 75 mm/s, and thus this value was selected for the subsequent tests, Fig. 3A. By fixing the scan speed at 75 mm/s, the effect of laser power was then studied and shown in Fig. 3B. For laser powers less than 1.75 W the beam energy was insufficient to form a uniform rGO reduction, while powers greater than 2 W led to the burning of the GO layer. The usable range was between 1.8 and 1.95 W, and in particular Fig. 3B shows the electrode conductivity reaching a maximum value of about 350 S/m for 1.85 W laser power. Thus, this value was thus selected as the optimum one and resulted in excellent conductivity when compared to unreduced GO, ~ 10^{-3} S/m.

To further confirm these results, the electrochemical active surface

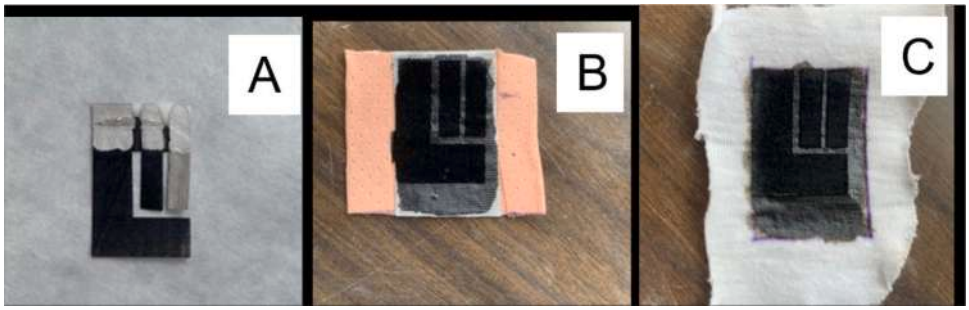

Fig. 5. A) Final configuration of the paper-based sensor. B) Sensor obtained on a commercial band-aid and C) textile.

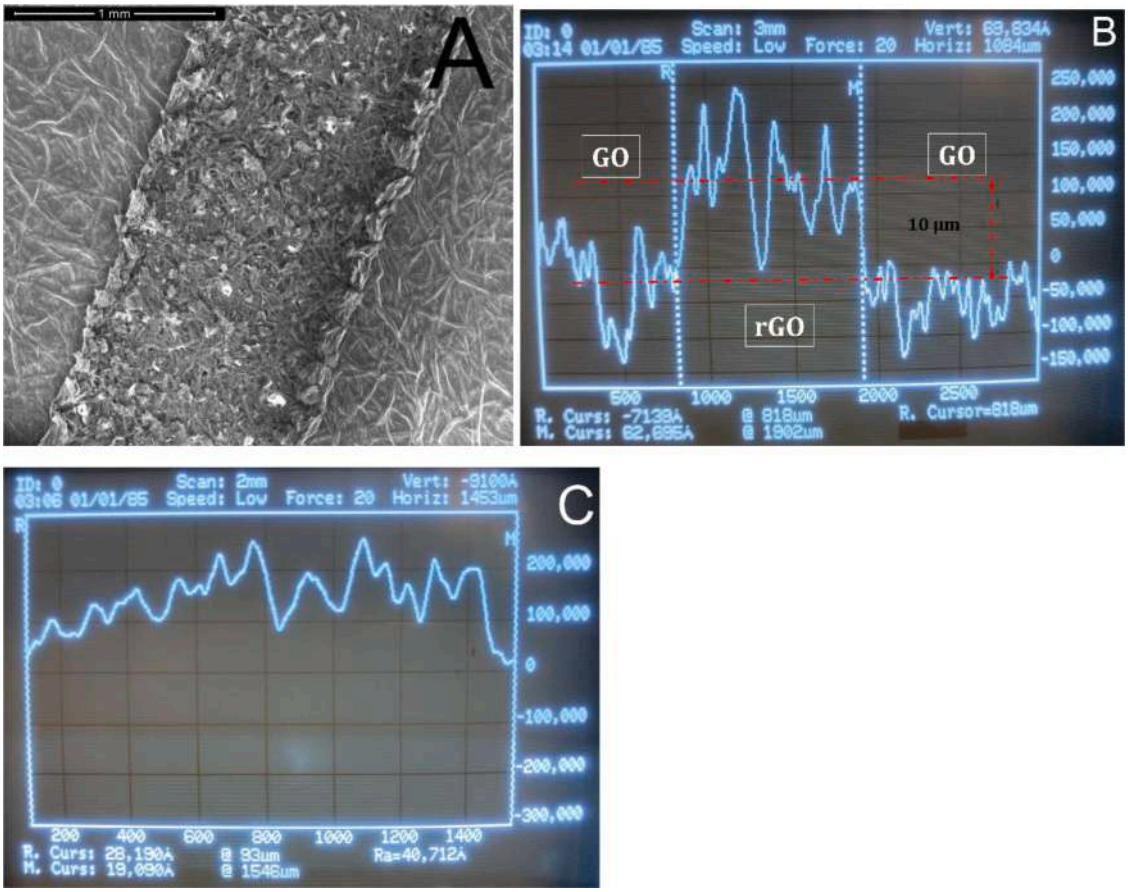

Fig. 6. A) SEM image of the rGO stripe (1 mm width). B) Surface profile of the rGO stripe (1 mm width) on GO substrate. C) Average surface roughness (Ra) of the rGO stripe.

area (ECSA) of the working electrodes were estimated. The ESCA was evaluated using the double-layer capacitance method and thus cyclic voltammetry (CV), at different scan rates, was performed in phosphate buffer solution (PBS, pH 7.4) in the potential range where no faradaic reactions occur, Fig. 4A.

Both anodic and cathodic capacitive currents increased with increasing scan rate. This suggests that the electrode has a capacitive behavior, typical of non-Faradaic regions of the voltammogram. The same behavior was found for three filter volumes of GO solution. Figure 4B shows the difference between anodic and cathodic currents (measured at 0.3 V vs Ag/AgCl) for each scan rate where a linear increase with the scan rate was observed. For each scan rate value, the Δj increased linearly with increasing volumes of GO. These experiments were carried out using electrodes fabricated by keeping both the scanning speed and the laser power constant; which influence the type of roughness of the rGO film. Consequently, for the same roughness factor, the increase in surface area is attributed to the increase in GO content. The slope of Δj lines vs scan rates represents the double-layer capacitance that is directly correlated to the ESCA. The slopes increased when increasing filtered volume of GO solution from 1.08, 1.43 and 1.96 mF cm^{-2} for 5, 10 and 20 mL respectively (+81% from 5 to 20 mL). Thus the ESCA of the electrode increased by increasing the filtering volume. This is a further confirmation that the best electrode was obtained for 20 mL of GO filter solution.

The image in Fig. 5A shows the final configuration of a sensor where it can be observed that the reference area has already been coated with Ag/AgCl paste while the contact pads of the three electrodes are coated with Ag paste. While in this work, the entire fabrication process was undertaken using filterpaper, it is important to point out that the same method can be used with other kinds of porous substrates. To this end, we also used a commercial band-aid (Fig. 5B) and a common textile (Fig. 5C) as substrates for sensor fabrication. Hence this fabrication method is highly flexible and adaptable because it allows the creation of sensors on different substrates of shapes and sizes that can be adjusted according to the application needs.

Optimized sensors were characterized by SEM, EDS, XRD, XPS and RAMAN. Figure 6A shows a SEM image after laser reduction with the equivalent surface profile presented in Fig. 6B. Both the reduced (central strip of Fig. 6A) and non-reduced areas of GO are clearly visible. From Fig. 6B a mean rGO thickness of about 10 µm was estimated. In the unreduced regions, a very compact and uniform GO film and the fibers of the paper support are visible. The morphology of the reduced areas appeared completely different, showing an extremely rough surface (Fig. 6A), and fibers from the underlying paper support can no longer be seen. The high roughness of the electrode surface provides a high surface area. Surface profilometry, showed that the average surface roughness (Ra) increased from 2 to 3 µm to 4 to 5 µm when movng from Go to rGO layers, respectively.

Fig. 7A shows the EDS spectrum recorded in the reduced (red curve) and un-reduced (black curve) areas of the surface. It can be observed that the reducing process leads to a lower oxygen content confirming the reduction of GO. In particular, the O/(C + O) ratio was ~0.239 in the unreduced GO while is ~ 0.099 in the rGO area with a decrease of about 59%. EDS was performed at several points of the sample and the ratio values presented are a mean value with a standard deviation of 1%. The corresponding Raman spectra are shown in Fig. 7B. The sample surfaces were analyzed at several points to verify their homogeneity using a very low laser power (about 4 mW) to prevent modifications of the sample surface due to laser irradiation (514 nm). The spectrum of GO (red line) shows two main peaks, at ~ 1343 and 1588 cm^{-1}. These two peaks are

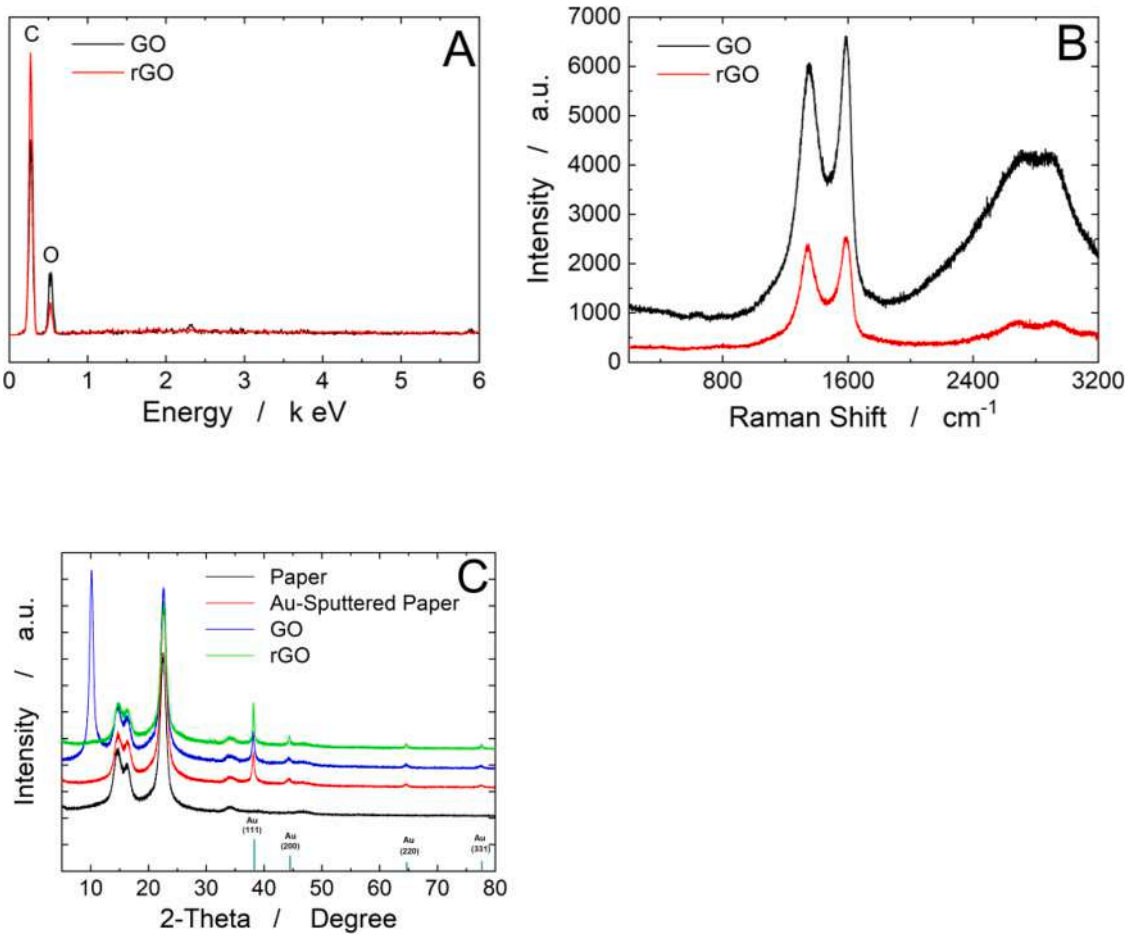

Fig. 7. A) EDS and B) RAMAN spectra of un-reduced and reduced GO. C) XRD patterns at different steps of the fabrication process.

attributed to the D and G Raman bands. Moreover, the 2D and S3 modes are clearly visible at ~2700 and 2930 cm^{-1} respectively [105–107]. The Raman spectrum of the rGO (blue curve) exhibits the same peaks, although with different intensities. As reported in the literature, the ratio between the intensity of the D and G bands can be used to quantify the degree of reduction of the GO [108,109]. Particularly, the I_D/I_G of the un-reduced GO is 0.905 while for the rGO a value of 0.95 was calculated. This increase in I_D/I_G is due to lower structural sp^3 defects confirming the reduction of the GO layer [110]. As reported in [104], the decrease of amorphous 2D and S3 modes suggests that the laser reduction is localized and does not lead to a large graphene planar sheet. Using the I_D/I_G ratio the estimation of crystallite sizes (L_a) can be undertaken using Eq. (3)

$$L_a(nm) = (2.4\ x\ 10^{-10}) x\ \lambda_L^4\ x\ \left(\frac{I_D}{I_G}\right)^{-1} \quad (3)$$

where λ_L is the wavelength of the Raman laser (514 nm in our case) [111]. Mean values of 18.51 and 17.63 nm were calculated for the film before and after reduction, respectively. Fig. 7C shows the XRD patterns of sensor at different stages of the fabrication process. In the diffraction pattern of the paper substrate (black curve) the diffraction peaks located at 14.65, 16.3, 22.55, 34.13 and 46.83 correspond to the polycrystalline cellulose (XRD card 056-1717) [112].

After the gold sputtering (red curve), new peaks appear located at 38.13, 44.13, 64.58 and 77.64 related to gold (111), (200), (220) and (311) planes, respectively (XRD card 04–784). In the pattern after GO filtration, a new peak at about 10.11 appears which is typical of the (002) plane of GO (blue curve). Finally, after the reduction of GO by means of the CO_2 laser (green curve), the (002) peak of GO almost disappears demonstrating the effective reduction of GO to rGO FP [113]. Unfortunately, the characteristic peak of rGO, located at about 22°, overlaps with the peak of cellulose and consequently cannot be identified.

The bonding configuration of carbon and oxygen before and after the laser treatment was investigated through XPS, Fig. 8. The analysis was carried out at three different points and results show that the GO film was quite homogeneous, as a close overlap of the observed peaks was observed. The analysis of the surface average composition revealed an O/C ratio of 0.32 (±0.003) with traces of S.

In the XPS spectrum of C 1s before laser reduction, Fig. 8A, C═C (284.50 eV, 46.46%), C—O—C (286.58 eV, 46.64%), and O—C═O (288.30 eV, 6.9%) bonds were identified [114]. In Fig. 8B the XPS spectrum of C 1s after laser treatment was reported. In the deconvoluted spectrum, the presence of the dominant peak of C═C (284.50 eV, 87.59%) and the shake-up satellite peak (π–π* transition, 290.82 eV) were identified [115]. The high intensity of C═C and the disappearance of C—O—C (286.58 eV) confirms the reduction of GO under laser irradiation[67,116]. Also, in this case, the sample was homogeneous and the analysis of the average composition of the surface revealed a decrease in the oxygen/carbon ratio (0.117 ± 0.015) with respect to the unreduced area. This decrease, of about 63%, was expected and confirms the EDS results. This was attributed to the removal of most of the carbonyl and hydroxyl groups due to the laser reduction [115,116].

The O 1s spectra before (Fig. 8C) and after (Fig. 8D) laser reduction was also studied. Before the reduction process, the O 1s spectra displayed the peaks at 530.93 (9.18%), 532.32 (83.55%), and 533.29 eV (7.27%) corresponding to C═O, O═C—OH and C—OH, respectively [117,118]. After reduction, C═O (530.21 eV, 20.90%), C—O (531.71

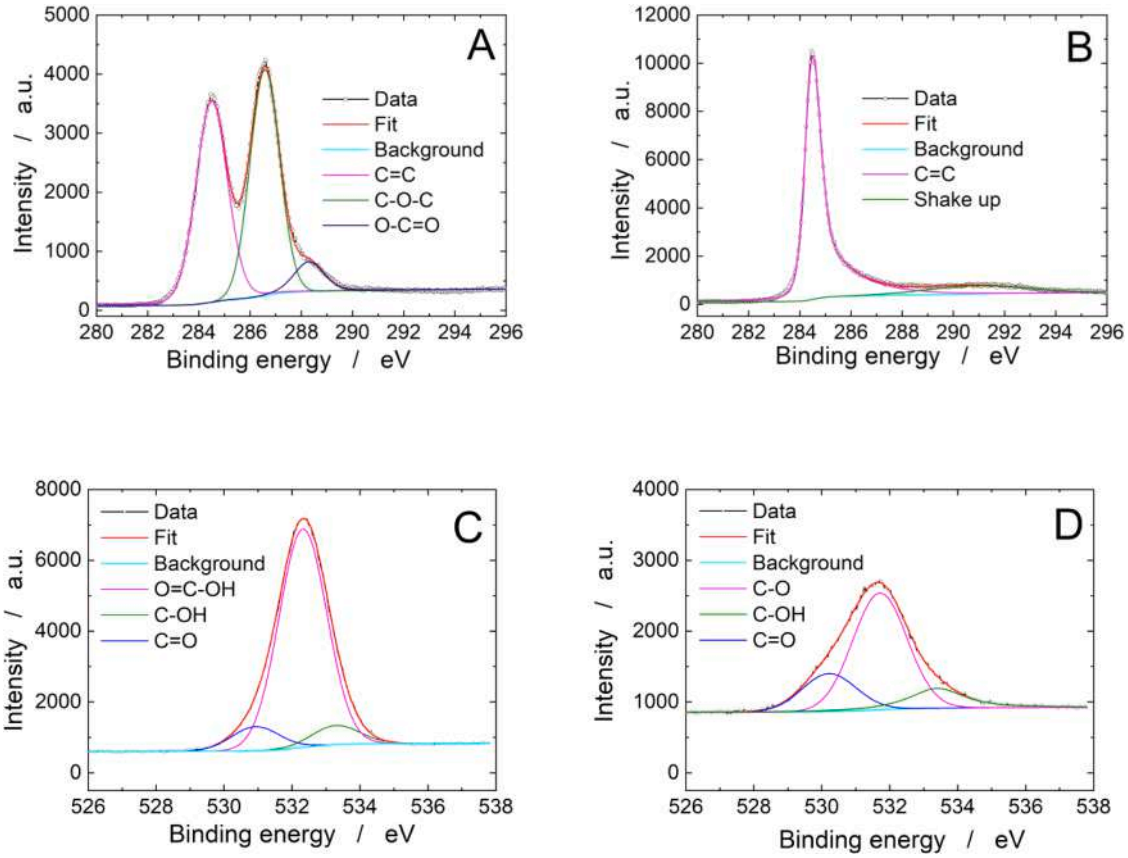

Fig. 8. XPS spectra of C 1s (A and B) and O 1s (C and D). A and C before laser reduction, B and D after laser reduction.

eV, 64.44%), and C—OH (533.40 eV, 14.66%) bonds were identified. The disappearance of the peak at 532.32 eV (corresponding to the COOH groups) in favor of the peak at 531.71 eV (relative to C—O) is a further clear indication of the reduction of GO due to the laser treatment [119].

3.2. Sensor performance

The electrochemical behavior of the electrode was studied by CVs performed in the potential range −0.5 to 0.5 V vs Ag/AgCl, using PBS with 0.05 M sulphuric acid, 0.1 mM ammonium molybdate and 0.005 mM phosphate. In Fig. 9, the CV curves in different conditions were reported. Fig. 9A shows the CV carried out in 0.05 M of sulphuric acid and in the absence of both molybdate and phosphate ions. The whole voltammogram is flat without any detectable peak, suggesting that at an electrode no redox reactions arising from H_2SO_4 occur in this potential range. After this test, 0.1 mM of ammonium molybdate was added to the sulphuric acid solution and a resulting CV is shown in Fig. 9B. In this case, the voltammogram is also flat. When phosphate ions were added to the solution (5 μM, Fig. 9C) three well-defined peaks, located at about +70 mV/+139 mV (I), −50 mV/+50 mV (II) and −137 mV/−60 mV (III) were present in the resulting CV. As reported by Nagul et al. [120], polyphosphomolybdate isomerizes into two different forms α (α-$[PMo_{12}O_{40}]^{3-}$) and β (β-$[PMo_{12}O_{40}]^{3-}$). Their concentration and stability depend on numerous parameters such as the concentration of molybdenum (VI) and phosphate anions, the acid concentration, the reaction time and temperature. The two isomers have very close oxidation/reduction potentials and as reported in [121–123], in the CVs 3 peaks can be found. The first and second are relative to the redox processes of the β-$[PMo_{12}O_{40}]^{3-}$ anion, while the second and third are due to the redox processes of α-$[PMo_{12}O_{40}]^{3-}$.

The calibration line of the proposed sensor for phosphate ion quantification was obtained using CV as a detection technique. CV was performed with a scan rate of 25 mV/sec. This scan speed was selected because the formation of well-defined peaks was observed even for low concentrations of the target analyte and while also ensuring the analysis time was not excessive.

Among the three peaks present in the CV curves, the more sensitive to the increment of phosphate ion concentration is that located at −50/+50 mV relative to the electrochemical reduction of Mo(VI) to Mo(IV). We observed that for this peak couple, the reduction peaks had a higher sensitivity toward the variation of phosphate ion concentration. Thus, the peak current of this reduction was used as the sensor readout (Fig. 9D). From Fig. 9D, the calibration line performing these experiments 3 times and using 3 different sensors was determined. The obtained results are shown in Fig. 10.

The sensor current density response increases with phosphate concentration with a reproducibility of 7.2% among the different experiments. The sensor response has two linear regions for phosphate concentration in the range from 1 to 20 μM (Fig. 10B) and also in the range from 20 to 100 μM (inset Fig. 10B) with the latter exhibiting a lower sensitivity. A plateau was reached for phosphate ions concentration higher than 1 mM.. Since the PMB formation follows reaction 1 in which the stoichiometry between molybdate and phosphate ions is 1.71:1, using a fixed molybdate concentration of 0.1 mM, means that the molybdate acts as a limiting reagent when phosphate concentration approaches 57 μM.The limit of detection (LOD) of the sensosr was calculated using the following equation:

$$LOD = 3.3 * SD/S \quad (4)$$

where SD is the standard deviation of the blank and S is the average sensor sensitivity yielding a calculated LOD of 0.4 μM.

Sensor selectivity was studied using 0.05 mM of phosphate ions in presence of 0.5 mM of different interfering species. Fig. 11 shows the result of this experiment as the ratio between the peak current density in

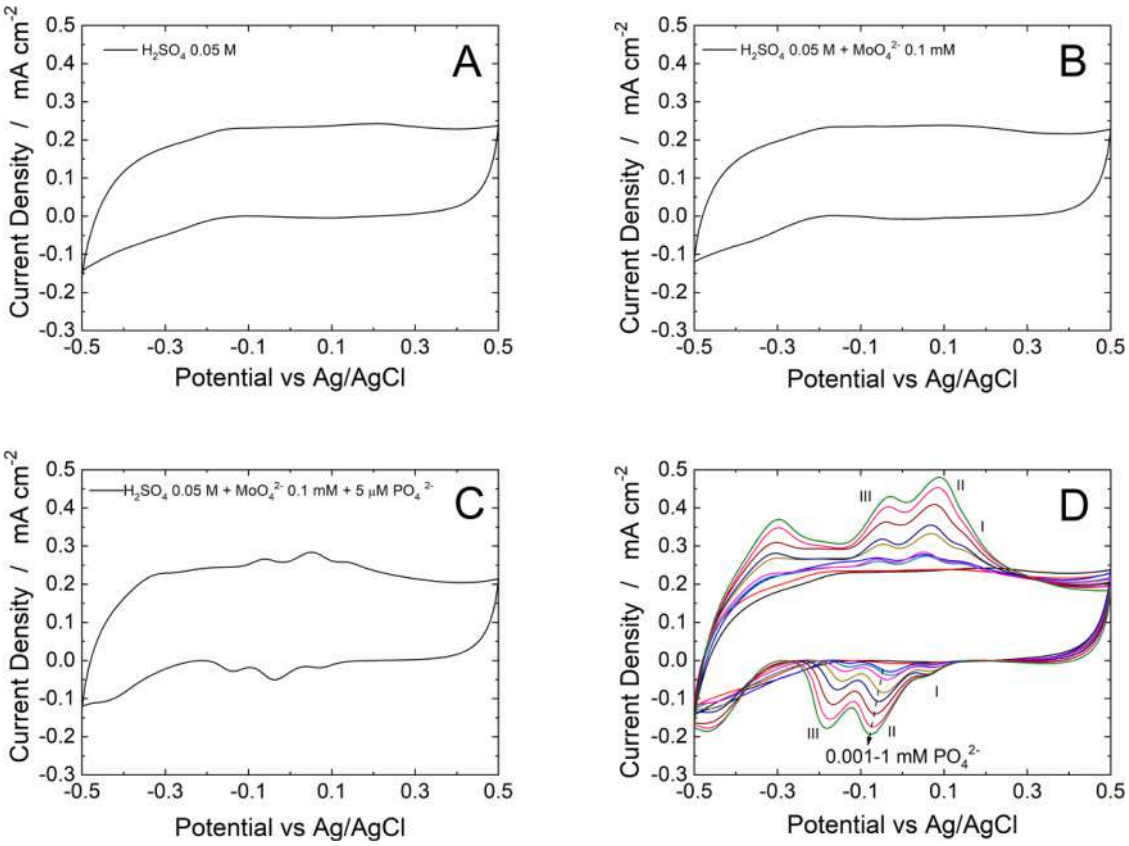

Fig. 9. CV in A) 0.05 M sulphuric acid, B) 0.05 M sulphuric acid and 0.1 mM ammonium molybdate, C) 0.05 M sulphuric acid, 0.1 mM ammonium molybdate and 0.005 mM phosphate, D) 0.05 M sulphuric acid, 0.1 mM ammonium molybdate and with increasing phosphate concentration from 1 to 1000 μM.

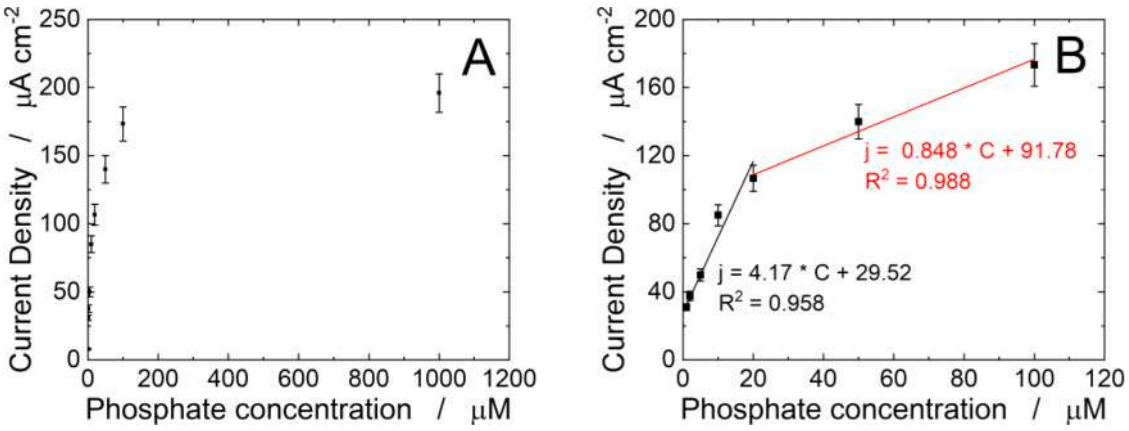

Fig. 10. A) Effect of phosphate concentration on the sensor readout. B) Corresponding calibration line.

the absence and presence of the interfering chemical species (nitrite, nitrate, lead, aluminum, zinc, potassium, iodide, copper, silicate and sodium ions).

Considering that the standard deviation of our sensor is ~ ±7.2% (dashed interval in Fig. 11), among the studied interfering species, only nitrate ions give an appreciable interference on the sensor output (~+22%). However, it is important to highlight that the maximum allowed concentration of nitrate ions in natural water is about 0.16 mM [124], almost three times lower than the concentration used in this work. Moreover, the real concentration of nitrate ions in natural waters is much lower than the maximum allowed concentration of 0.16 mM. Thus it is possible say that in most applications, that the proposed sensor is selective for phosphate detection.

To further validate the sensor, the quantification of phosphate ions in river water samples was undertaken. Water was collected from Oreto River (Palermo, Italy) and tested without any physical pretreatment. After acidification and the addition of ammonium molybdate (0.1 mM), CV was carried out and a small peak was detected (Fig. 12A, red curve), demonstrating that phosphate ions were present in the river water albeit at very low concentrations. Then, different concentrations of phosphate ions were spiked into the solution (Fig. 12A) and the standard addition method was used to quantify the unknown phosphate concentration (Fig. 12B). Using this approach, a concentration of phosphate ions of ~ 3.83 μM was determined. To confirm the results obtained using the sensors, the same river water samples were also analyzed using a standard colorimetric assay. Before analyzing the river water, the calibration

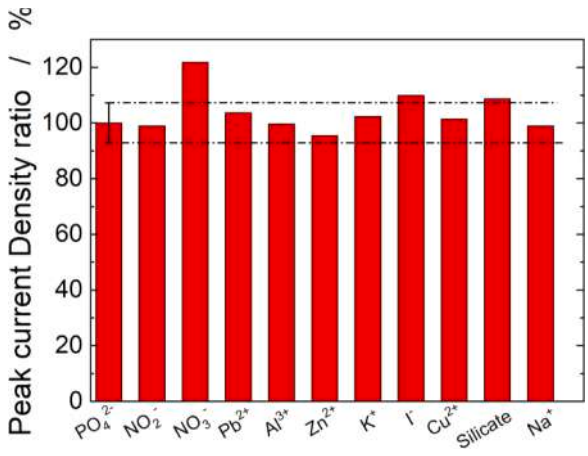

Fig. 11. Selectivity test.

line reported in Fig. 12C was determined. In the real sample, by colorimetric assay, a phosphate concentration of 2.91 μM was measured. Considering the dilution ratio of the sample for the colorimetric assay (130 μL of river water sample + 50 μL of molybdate + 20 μL of tin), the real concentration was estimated to be ~4.47 ± 0.6 μM. This result is very close to the value measured using our sensor, confirming its applicability to real water samples.

3.3. Ready to use sensor

The possibility of absorbing the chemicals, necessary for the formation of the Keggin's ion in, and their subsequently release from, thefilterpaper substrate, into a water sample was studied. Following fabrication, sensors were brought into contact with a solution of sulphuric acid and ammonium molybdate. Specifically, 10 μL/cm^2 of the solution was placed on the back of a sensor, so that it was absorbed by the FP substrate. The sensors were then left to dry at 60 °C in an air-vented oven. To study the release of H^+, the dried sensors were immersed in 1 mL of deionized water and the pH was monitored over time; using a standard pH meter. The concentration of sulphuric acid in the absorbed solution was optimized to achieve a final pH =1.56, equal to the solution pH of 0.05 M sulphuric acid used for the tests described above. It was observed that sulphuric acid concentrations higher than 2 M cannot be used because they are too aggressive for the paper substrate which tended to dissolve at these high concetrations. Varying the H_2SO_4 concentration from 0.05 M to 2 M we found that the pH of deionized water reached a plateau after 120/180 s of immersion shown in Fig. 13A showing the rapid acidifcation of the sample.By increasing the H_2SO_4 concentration, a lower final pH was achieved. Specifically, as shown in the inset of Fig. 13A, a final pH of 1.62, 1.54, 1.45 and 1.19 was measured for 0.5, 0.75, 1 and 2 M of sulphuric acid, respectively. Thus it can be concluded that to reach a final pH of 1.56 an adsorbing concentration of 0.75 M.sulphuric acid was required

Experiments were carried out by absorbing 10 μL/cm^2 of a solution of ammonium molybdate at different concentrations (2.5, 5, 7.5, 10, 15 and 20 mM). Following absorption of these solutions and allowed to completely dry, sensors were immersed in 1 mL of deionized water and the amount of released molybdate ions quantified using a colorimetric assay. The subsequent calibration line for MoO_4^{2-}, is presented in Fig. 13B. For this purpose, the colorimetric assay was carried out with a large excess of phosphate ions and the same concentration of tin chloride, while molybdate was spiked at different concentrations, from 0.05 to 0.5 mM. As can be observed in Fig. 13B, the absorbance of the solution increased linearly with increasing molybdate concentration (abs = 0.847*C + 0.0727). For this calibration line, the absorbance of a solution of 0.1 mM of molybdate ions (used in the assyas presented in Fig. 10 above) was equal to 0.156. Thus, this value served as a reference to determine the right concentration of molybdate ions that must be adsorbed and subsequently released into a a sample by a sensor. Different solutions with released molybdate ions were prepared and mixed with phosphate, tin and chloride ions and the absorbance was

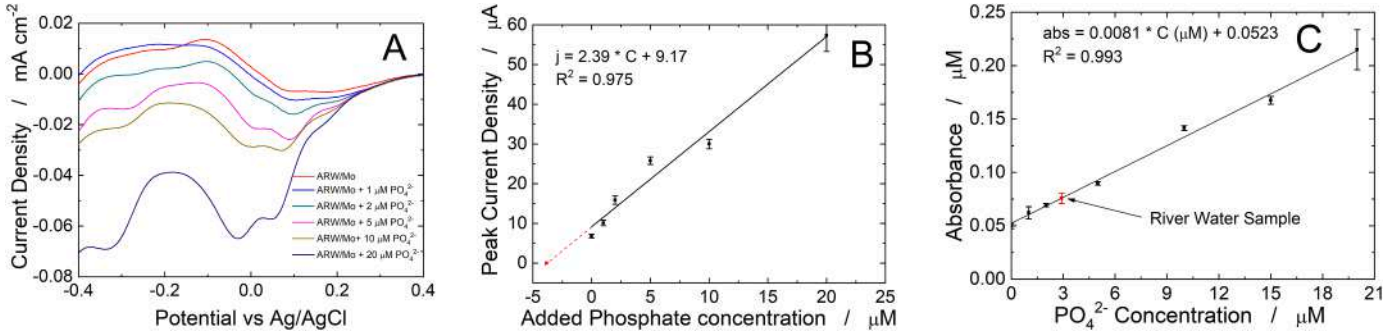

Fig. 12. Analysis of acidified river water (ARW) containing 0.1 mM of ammonium molybdate (ARW/Mo). A) Effect of increasing concentration of phosphate ions using ARW/Mo as solution. B) Corresponding calibration line using standard addition method. C) Phosphate detection in river water using a standard colorimetric assay.

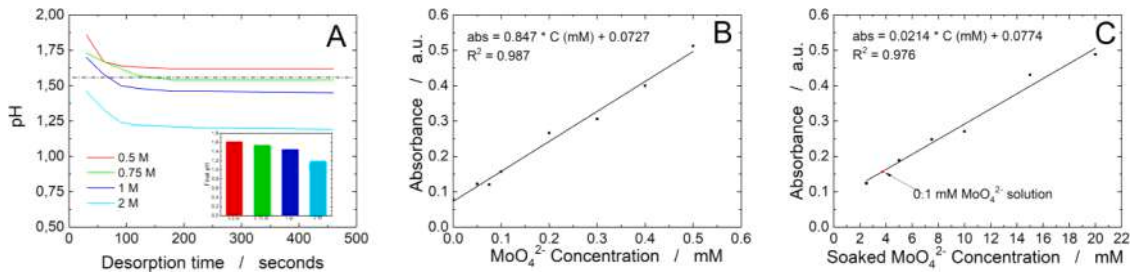

Fig. 13. A) pH curves relative to the release of sulfuric acid from the paper substrate of the sensor. B) Calibration line for molybdate ions. (C) Molybdate ions quantification released from the paper substrate of the sensor.

Table 1
Comparison with literature data.

Electrode	Electrochemical Technique	Source of molybdate and protons	Linear Range μM	Limit of Detection μM	Sensitivity μA^{-1} μM cm^{-2}	Real Sample	Ref
PtAu NWs	CH	Molybdate in solution	248–1456	45	0.0505	Pond Water	[125]
Screen-printed graphite macroelectrodes	CV	Molybdate and H_2SO_4 in solution	0.003–0.115 μM	0.002 μM	5.92 μA/μM	Canal water	[126]
Carbon black	CV	Paper impregnation	10–300	4	1.62* esteemed	River Water	[62]
rGOOMC/SPE	DPV	Molybdate in solution	0.2–150	0.05	11.46	Sea Water	[56]
Rotating Au Electrode	CH	In situ production of molybdate	0.33–3.2	0.12	0.2439	Sea Water	[127]
PGE	DPV	Molybdate in solution	10–100	1.25	19.41	Soil	[63]
CP-Microelectrodes	CH	Molybdate in solution	1–20	0.3	N.S.	Seawater	[128]
GC-PB	DPV	Molybdate in solution	500–5000	38.3	0.261	Biodisel	[129]
LsRGO	**CV**	**Paper impregnation**	**1–20**	**0.4**	**4.17**	**River Water**	**This work**

NWs: Nanowires, rGO: reduced graphene oxide, PGE: pencil graphite electrode, CP: Carbon Paste, GC: Glassy Carbon, PB: Prussian Blue, LsRGO: Laser scribed reduced graphene oxide, CH: chronoamperometry, CV: cyclic voltammetry, DPV: differential pulse voltammetry, N.S.: not shown.

measured. Figure 13C shows that the increase in abosrbance observed with increasing concentrations of molybdate in the soaking solutions (abs = 0.0214*C + 0.0774). From these data, we determined that a soaking solution with a concentration of 3.67 mM of ammonium molybdate was enough to release 0.1 mM of MoO_4^{2-}, into a water sample (1 mL). These experiments clearly demonstrate the ability of the proposed sensor to absorb the required chemicals and quantify phosphate ions without the need to add any reagent.

In Table 1 the performance of the proposed sensor was compared with other published electrochemical sensors based on the molybdenum blu method. It can be observed that our sensor exhibited higher sensitivity with respect to other other works. Also the LOD and linear range are highly satisfying. In addition, the data reported in Table 1 show that our sensor can work without adding any reagent to the sample to be analyzed, unlike many other works which require modification of the solution with the addition of molybdate and sulphuric acid.

4. Conclusions

In this work, an easy method for fabrication of sensors based on reduced graphene oxide through the use of a CO_2 laser is reported. The process was optimized using filterpaper but preliminary results show that it is also easily adaptable to many other types of porous substrate, such as a band-aid orfabric. The whole process is scalable, fast, economical, and easy to carry out with the developed sensors applicable to many different fields. The active material of the sensor is the reduced graphene oxide which has been shown to be an ideal active material for the detection of different analytes. The process led to the formation of a complete sensor consisting of working, counter and reference electrodes. In this work, different process parameters (GO concentration, laser speed, laser power) were optimized to yield highly performing, stable and reproducible sensors. The developed sensors were used to quantify phosphate ions in water samplesbased on the reaction between molybdate and phosphate in acidic media and the subsequent formation of the Keggin-type complex $PMo_{12}O_{40}^{3-}$. The sensors enabled detection of phosphate ions in a wide linear range: from 1 to 20 μM with a LOD of 0.4 μM, and were selective to phosphate Sensors were validated using real samples (water river) and the results were benchmared against, and behnaved favourable to standard colorimetric technique

To eliminate the need for water sample pretreatment, ready-to-use sensors were demonstrated to be directly suitable for the detection of phosphate ions in the field by pre-impregnated them with sulphuric acid and molybdate solutions. During sensor operation, these chemicals were released directly into the water sample to be analyzed prior to the phosphate test. Thus, fabrication of a portable, easy-to-use and fast phosphate sensor for in situ and real-time monitoring of water quality was here demonstrated.

CRediT authorship contribution statement

Bernardo Patella: Investigation, Writing – original draft, Methodology, Writing – review & editing. **Antonino Parisi:** Investigation, Writing – original draft, Methodology. **Nadia Moukri:** Investigation, Methodology. **Federico Gitto:** Investigation, Methodology. **Alessandro Busacca:** Conceptualization, Supervision. **Giuseppe Aiello:** Conceptualization, Supervision. **Michele Russo:** Supervision, Funding acquisition. **Alan O'Riordan:** Supervision, Writing – review & editing. **Rosalinda Inguanta:** Conceptualization, Writing – review & editing, Funding acquisition, Supervision.

Declaration of Competing Interest

The authors declare the following financial interests/personal relationships which may be considered as potential competing interests: Rosalinda Inguanta reports financial support was provided by University of Palermo. Alan O'Riordan reports financial support was provided by Tyndall National Institute. Michele Russo reports financial support was provided by Dipietro group.

Data Availability

No data was used for the research described in the article.

Acknowledgments

This work was supported by the University of Palermo, Tyndall National Institute and Dipietro Group.

References

[1] A.L. Srivastav, M. Ranjan, Inorganic Water Pollutants. Inorganic Pollutants in Water, Elsevier, 2020, pp. 1–15, https://doi.org/10.1016/B978-0-12-818965-8.00001-9.
[2] Role of inorganic pollutants in freshwater ecosystem- a review, Int. J. Adv. Res. Biol. Sci. (n.d.).
[3] L. Jiao, N. Zhong, X. Zhao, S. Ma, X. Fu, D. Dong, Recent advances in fiber-optic evanescent wave sensors for monitoring organic and inorganic pollutants in water, TrAC Trends Anal. Chem. 127 (2020), 115892, https://doi.org/10.1016/j.trac.2020.115892.
[4] B.L. Rivas, B.F. Urbano, J. Sánchez, Water-Soluble and insoluble polymers, nanoparticles, nanocomposites and hybrids with ability to remove hazardous inorganic pollutants in water, Front. Chem. 6 (2018) 320, https://doi.org/10.3389/fchem.2018.00320.

[5] M. Abdelwaheb, K. Jebali, H. Dhaouadi, S. Dridi-Dhaouadi, Adsorption of nitrate, phosphate, nickel and lead on soils: risk of groundwater contamination, Ecotoxicol. Environ. Saf. 179 (2019) 182–187, https://doi.org/10.1016/j.ecoenv.2019.04.040.

[6] M.K. Sharma, M. Kumar, Sulphate contamination in groundwater and its remediation: an overview, Environ. Monit. Assess. 192 (2020) 74, https://doi.org/10.1007/s10661-019-8051-6.

[7] S. Ali, S.K. Thakur, A. Sarkar, S. Shekhar, Worldwide contamination of water by fluoride, Environ. Chem. Lett. 14 (2016) 291–315, https://doi.org/10.1007/s10311-016-0563-5.

[8] J.U. Ahmad, Md.A. Goni, Heavy metal contamination in water, soil, and vegetables of the industrial areas in Dhaka, Bangladesh, Environ. Monit. Assess. 166 (2010) 347–357, https://doi.org/10.1007/s10661-009-1006-6.

[9] R. Lindström, A system for modelling groundwater contamination in water supply areas: chloride contamination from road de-icing as an example, Hydrol. Res. 37 (2006) 41–51, https://doi.org/10.2166/nh.2006.0004.

[10] P.N. Okafor, U.I. Ogbonna, Nitrate and nitrite contamination of water sources and fruit juices marketed in South-Eastern Nigeria, J. Food Compos. Anal. 16 (2003) 213–218, https://doi.org/10.1016/S0889-1575(02)00167-9.

[11] A.R. Satayeva, C.A. Howell, A.V. Korobeinyk, J. Jandosov, V.J. Inglezakis, Z. A. Mansurov, S.V. Mikhalovsky, Investigation of rice husk derived activated carbon for removal of nitrate contamination from water, Sci. Total Environ. 630 (2018) 1237–1245, https://doi.org/10.1016/j.scitotenv.2018.02.329.

[12] D. Vashisht, A. Kumar, S.K. Mehta, A. Ibhadon, Analysis of emerging contaminants: a case study of the underground and drinking water samples in Chandigarh, India Environ. Adv. 1 (2020), 100002, https://doi.org/10.1016/j.envadv.2020.100002.

[13] S.N. Zulkifli, H.A. Rahim, W.-J. Lau, Detection of contaminants in water supply: a review on state-of-the-art monitoring technologies and their applications, Sens. Actuators B Chem. 255 (2018) 2657–2689, https://doi.org/10.1016/j.snb.2017.09.078.

[14] S.D. Richardson, S.Y. Kimura, Water analysis: emerging contaminants and current issues, Anal. Chem. 92 (2020) 473–505, https://doi.org/10.1021/acs.analchem.9b05269.

[15] C. Cipollina, A. Bruno, S. Fasola, M. Cristaldi, B. Patella, R. Inguanta, A. Vilasi, G. Aiello, S.L. Grutta, C. Torino, E. Pace, Cellular and molecular signatures of oxidative stress in bronchial epithelial cell models injured by cigarette smoke extract, Int. J. Mol. Sci. (2022) 22.

[16] B. O'Sullivan, S. O'Sullivan, T. Narayan, H. Shao, B. Patella, I. Seymour, R. Inguanta, A. O'Riordan, A direct comparison of 2D versus 3D Diffusion analysis at nanowire electrodes: a finite element analysis and experimental study, Electrochim. Acta (2022), 139890, https://doi.org/10.1016/j.electacta.2022.139890.

[17] S. Krishnan, Review—electrochemical sensors for large and small molecules in biofluids, J. Electrochem. Soc. 167 (2020), 167505, https://doi.org/10.1149/1945-7111/abcbb5.

[18] D.W. Kimmel, G. LeBlanc, M.E. Meschievitz, D.E. Cliffel, Electrochemical sensors and biosensors, Anal. Chem. 84 (2012) 685–707, https://doi.org/10.1021/ac202878q.

[19] B. O'Sullivan, B. Patella, R. Daly, I. Seymour, C. Robinson, P. Lovera, J. Rohan, R. Inguanta, A. O'Riordan, A simulation and experimental study of electrochemical pH control at gold interdigitated electrode arrays, Electrochim. Acta 395 (2021), 139113, https://doi.org/10.1016/j.electacta.2021.139113.

[20] B. Patella, N. Moukri, G. Regalbuto, C. Cipollina, E. Pace, S. Di Vincenzo, G. Aiello, A. O'Riordan, R. Inguanta, Electrochemical synthesis of zinc oxide nanostructures on flexible substrate and application as an electrochemical immunoglobulin-G immunosensor, Materials (Basel) 15 (2022) 713, https://doi.org/10.3390/ma15030713.

[21] K. Dawson, A. Wahl, S. Barry, C. Barrett, N. Sassiat, A.J. Quinn, A. O'Riordan, Fully integrated on-chip nano-electrochemical devices for electroanalytical applications, Electrochim. Acta 115 (2014) 239–246, https://doi.org/10.1016/j.electacta.2013.10.144.

[22] M. Ben Jaballah, A. Ambily Rajendran, B. Prieto-Simón, C. Dridi, Development of a sustainable nanosensor using green Cu nanoparticles for simultaneous determination of antibiotics in drinking water, Anal. Methods 14 (2022) 2014–2025, https://doi.org/10.1039/D2AY00419D.

[23] B. Patella, G. Aiello, G. Drago, C. Torino, A. Vilasi, A. O'Riordan, R. Inguanta, Electrochemical detection of chloride ions using Ag-based electrodes obtained from compact disc, Anal. Chim. Acta 1190 (2022), 339215, https://doi.org/10.1016/j.aca.2021.339215.

[24] P.K. Kalambate, Z. Rao, J.Wu Dhanjai, Y. Shen, R. Boddula, Y. Huang, Electrochemical (bio) sensors go green, Biosens. Bioelectron. 163 (2020), 112270, https://doi.org/10.1016/j.bios.2020.112270.

[25] H. Shi, L. Fu, F. Chen, S. Zhao, G. Lai, Preparation of highly sensitive electrochemical sensor for detection of nitrite in drinking water samples, Environ. Res. 209 (2022), 112747, https://doi.org/10.1016/j.envres.2022.112747.

[26] B. Patella, S. Piazza, C. Sunseri, R. Inguanta, Nio thin film for mercury detection in water by square wave anodic stripping voltammetry, Chem. Eng. Trans. 60 (2017) 1–6, https://doi.org/10.3303/CET1760001.

[27] L.A. Wasiewska, I. Seymour, B. Patella, R. Inguanta, C.M. Burgess, G. Duffy, A. O'Riordan, Reagent free electrochemical-based detection of silver ions at interdigitated microelectrodes using in-situ pH control, Sens. Actuators B Chem. 333 (2021), 129531, https://doi.org/10.1016/j.snb.2021.129531.

[28] R.J. Davenport, D.C. Johnson, Voltammetric determination of nitrate and nitrite ions using a rotating cadmium disk electrode, Anal. Chem. 45 (1973) 1979–1980, https://doi.org/10.1021/ac60333a038.

[29] E. Bernalte, S. Arévalo, J. Pérez-Taborda, J. Wenk, P. Estrela, A. Avila, M. Di Lorenzo, Rapid and on-site simultaneous electrochemical detection of copper, lead and mercury in the Amazon river, Sens. Actuators B Chem. 307 (2020), 127620, https://doi.org/10.1016/j.snb.2019.127620.

[30] P. Gołębiewski, B. Puciłowski, F. Sommer, S. Kubik, M. Daniels, W. Dehaen, U. Sivasankaran, K.G. Kumar, H. Radecka, J. Radecki, Electrochemical sensing of sulfate in aqueous solution with a cyclopeptide-dipyrromethene-Cu(II) or Co(II) complex attached to a gold electrode, Sens. Actuators B Chem. 285 (2019) 536–545, https://doi.org/10.1016/j.snb.2019.01.083.

[31] L.A. Romero-Cano, A.I. Zárate-Guzmán, F. Carrasco-Marín, L.V. González-Gutiérrez, Electrochemical detection of copper in water using carbon paste electrodes prepared from bio-template (grapefruit peels) functionalized with carboxyl groups, J. Electroanal. Chem. 837 (2019) 22–29, https://doi.org/10.1016/j.jelechem.2019.02.005.

[32] N.-U.-A. Babar, K.S. Joya, M.A. Tayyab, M.N. Ashiq, M. Sohail, Highly sensitive and selective detection of arsenic using electrogenerated nanotextured gold assemblage, ACS Omega 4 (2019) 13645–13657, https://doi.org/10.1021/acsomega.9b00807.

[33] A. Maikap, K. Mukherjee, N. Mandal, B. Mondal, A.K. Meikap, Iron (III) oxide hydroxide based novel electrode for the electrochemical detection of trace level fluoride present in water, Electrochim. Acta 264 (2018) 150–156, https://doi.org/10.1016/j.electacta.2018.01.055.

[34] B. Patella, T. Narayan, B. O'Sullivan, R. Daly, C. Zanca, P. Lovera, R. Inguanta, A. O'Riordan, Simultaneous detection of copper and mercury in water samples using in-situ pH control with electrochemical stripping techniques, Electrochim. Acta 439 (2023), 141668, https://doi.org/10.1016/j.electacta.2022.141668.

[35] K. Białas, D. Moschou, F. Marken, P. Estrela, Electrochemical sensors based on metal nanoparticles with biocatalytic activity, Microchim. Acta 189 (2022) 172, https://doi.org/10.1007/s00604-022-05252-2.

[36] C. Zhu, G. Yang, H. Li, D. Du, Y. Lin, Electrochemical sensors and biosensors based on nanomaterials and nanostructures, Anal. Chem. 87 (2015) 230–249, https://doi.org/10.1021/ac5039863.

[37] G.B. Darband, M. Aliofkhazraei, S. Shanmugam, Recent advances in methods and technologies for enhancing bubble detachment during electrochemical water splitting, Renew. Sustain. Energy Rev. 114 (2019), 109300, https://doi.org/10.1016/j.rser.2019.109300.

[38] B. Buccheri, F. Ganci, B. Patella, G. Aiello, P. Mandin, R. Inguanta, Ni-Fe alloy nanostructured electrodes for water splitting in alkaline electrolyser, Electrochim. Acta 388 (2021), 138588, https://doi.org/10.1016/j.electacta.2021.138588.

[39] H. Yin, C. Zhang, X. Bai, Z. Yang, Z. Liu, Tuning electrochemical properties of silver nanomaterials by doping with boron: application for highly non-enzymatic sensing of hydrogen peroxide, ChemistrySelect 7 (2022), https://doi.org/10.1002/slct.202201310.

[40] L. Silipigni, F. Barreca, E. Fazio, F. Neri, T. Spanò, S. Piazza, C. Sunseri, R. Inguanta, Template electrochemical growth and properties of Mo oxide nanostructures, J. Phys. Chem. C. 118 (2014) 22299–22308, https://doi.org/10.1021/jp505819j.

[41] J.-J. Xu, N. Bao, X.-H. Xia, Y. Peng, H.-Y. Chen, Electrochemical detection method for nonelectroactive and electroactive analytes in microchip electrophoresis, Anal. Chem. 76 (2004) 6902–6907, https://doi.org/10.1021/ac0490595.

[42] B. Kaur, C.A. Erdmann, M. Daniëls, W. Dehaen, Z. Rafiński, H. Radecka, J. Radecki, Highly sensitive electrochemical sensor for the detection of anions in water based on a redox-active monolayer incorporating an anion receptor, Anal. Chem. 89 (2017) 12756–12763, https://doi.org/10.1021/acs.analchem.7b03001.

[43] A. Shvarev, E. Bakker, Reversible electrochemical detection of nonelectroactive polyions, J. Am. Chem. Soc. 125 (2003) 11192–11193, https://doi.org/10.1021/ja037167n.

[44] C. Forano, H. Farhat, C. Mousty, Recent trends in electrochemical detection of phosphate in actual waters, Curr. Opin. Electrochem. 11 (2018) 55–61, https://doi.org/10.1016/j.coelec.2018.07.008.

[45] U. Sivasankaran, L. Reinke, S.K. Anand, K. Malecka, K.G. Kumar, H. Radecka, S. Kubik, J. Radecki, Ultrasensitive electrochemical sensing of phosphate in water mediated by a dipicolylamine-zinc(II) complex, Sens. Actuators B Chem. 321 (2020), 128474, https://doi.org/10.1016/j.snb.2020.128474.

[46] https://www.fao.org/3/i7754e/i7754e.pdf, (n.d.).

[47] Md.R. Awual, Efficient phosphate removal from water for controlling eutrophication using novel composite adsorbent, J. Clean. Prod. 228 (2019) 1311–1319, https://doi.org/10.1016/j.jclepro.2019.04.325.

[48] S.P. Boeykens, M.N. Piol, L. Samudio Legal, A.B. Saralegui, C. Vázquez, Eutrophication decrease: phosphate adsorption processes in presence of nitrates, J. Environ. Manage. 203 (2017) 888–895, https://doi.org/10.1016/j.jenvman.2017.05.026.

[49] E. Rosales, G. Del Olmo, C. Calero Preciado, I. Douterelo, Phosphate dosing in drinking water distribution systems promotes changes in biofilm structure and functional genetic diversity, Front. Microbiol. 11 (2020), 599091, https://doi.org/10.3389/fmicb.2020.599091.

[50] D. Litke, Review of Phosphorus Control Measures in the United States and Their Effects on Water Quality, 1999. https://doi.org/10.3133/wri994007.

[51] Deirdre Tierney, Shane O'Boyle, Water Quality in 2016: An Indicators Report, n. d.

[52] A.T. Lawal, S.B. Adeloju, Progress and recent advances in phosphate sensors: a review, Talanta 114 (2013) 191–203, https://doi.org/10.1016/j.talanta.2013.03.031.

[53] S. Khoshniat, A. Bourgine, M. Julien, P. Weiss, J. Guicheux, L. Beck, The emergence of phosphate as a specific signaling molecule in bone and other cell types in mammals, Cell. Mol. Life Sci. 68 (2011) 205–218, https://doi.org/10.1007/s00018-010-0527-z.
[54] S. Ganesh, F. Khan, M.K. Ahmed, P. Velavendan, N.K. Pandey, U.K. Mudali, Spectrophotometric determination of trace amounts of phosphate in water and soil, Water Sci. Technol. 66 (2012) 2653–2658, https://doi.org/10.2166/wst.2012.468.
[55] S. Pradhan, M.R. Pokhrel, Spectrophotometric determination of phosphate in sugarcane juice, fertilizer, detergent and water samples by molybdenum blue method, Sci. World 11 (2013) 58–62, https://doi.org/10.3126/sw.v11i11.9139.
[56] H. Wei, D. Pan, Z. Zhou, H. Han, R. Zhu, On-site electrochemical determination of phosphate with high sensitivity and anti-interference ability in turbid coastal waters, Ecotoxicol. Environ. Saf. 221 (2021), 112444, https://doi.org/10.1016/j.ecoenv.2021.112444.
[57] S. Berchmans, T.B. Issa, P. Singh, Determination of inorganic phosphate by electroanalytical methods: a review, Anal. Chim. Acta 729 (2012) 7–20, https://doi.org/10.1016/j.aca.2012.03.060.
[58] A. Prasad, S.P. Sahu, S.K. Figueiredo Stofela, A. Chaichi, S.M.A. Hasan, W. Bam, K. Maiti, K.M. McPeak, G.L. Liu, M.R. Gartia, Printed electrode for measuring phosphate in environmental water, ACS Omega 6 (2021) 11297–11306, https://doi.org/10.1021/acsomega.1c00132.
[59] C. Warwick, A. Guerreiro, A. Soares, Sensing and analysis of soluble phosphates in environmental samples: a review, Biosens. Bioelectron. 41 (2013) 1–11, https://doi.org/10.1016/j.bios.2012.07.012.
[60] S. Sedaghat, S. Jeong, A. Zareei, S. Peana, N. Glassmaker, R. Rahimi, Development of a nickel oxide/oxyhydroxide-modified printed carbon electrode as an all solid-state sensor for potentiometric phosphate detection, New J. Chem. 43 (2019) 18619–18628, https://doi.org/10.1039/C9NJ04502C.
[61] L. Hsu, P.R. Selvaganapathy, Stable and reusable electrochemical sensor for continuous monitoring of phosphate in water, in: IEEE SENSORS 2014 Proceedings, IEEE, Valencia, Spain, 2014, pp. 1423–1426, https://doi.org/10.1109/ICSENS.2014.6985280.
[62] S. Cinti, D. Talarico, G. Palleschi, D. Moscone, F. Arduini, Novel reagentless paper-based screen-printed electrochemical sensor to detect phosphate, Anal. Chim. Acta 919 (2016) 78–84, https://doi.org/10.1016/j.aca.2016.03.011.
[63] M.B. Arvas, H. Gürsu, M. Gençten, Y. Sahin, Electrochemical formation of molybdenum phosphate on a pencil graphite electrode and its potential application for the detection of phosphate ions, Anal. Methods 10 (2018) 4282–4291, https://doi.org/10.1039/C8AY01653D.
[64] K.A. Madurani, S. Suprapto, N.I. Machrita, S.L. Bahar, W. Illiya, F. Kurniawan, Progress in graphene synthesis and its application: history, challenge and the future outlook for research and industry, ECS J. Solid State Sci. Technol. 9 (2020), 093013, https://doi.org/10.1149/2162-8777/abbb6f.
[65] E. Jaafar, M. Kashif, S.K. Sahari, Z. Ngaini, Study on morphological, optical and electrical properties of graphene oxide (GO) and reduced graphene oxide (rGO), MSF 917 (2018) 112–116, https://doi.org/10.4028/www.scientific.net/MSF.917.112.
[66] A.T. Dideikin, A.Y. Vul', Graphene oxide and derivatives: the place in graphene family, Front. Phys. 6 (2019) 149, https://doi.org/10.3389/fphy.2018.00149.
[67] S. Roy, N. Soin, R. Bajpai, D.S. Misra, J.A. McLaughlin, S.S. Roy, Graphene oxide for electrochemical sensing applications, J. Mater. Chem. 21 (2011) 14725, https://doi.org/10.1039/c1jm12028j.
[68] A.T. Smith, A.M. LaChance, S. Zeng, B. Liu, L. Sun, Synthesis, properties, and applications of graphene oxide/reduced graphene oxide and their nanocomposites, Nano Mater. Sci. 1 (2019) 31–47, https://doi.org/10.1016/j.nanoms.2019.02.004.
[69] V.V. Neklyudov, N.R. Khafizov, I.A. Sedov, A.M. Dimiev, New insights into the solubility of graphene oxide in water and alcohols, Phys. Chem. Chem. Phys. 19 (2017) 17000–17008, https://doi.org/10.1039/C7CP02303K.
[70] S. Pei, H.-.M. Cheng, The reduction of graphene oxide, Carbon N Y 50 (2012) 3210–3228, https://doi.org/10.1016/j.carbon.2011.11.010.
[71] F. Mazzara, B. Patella, G. Aiello, C. Sunseri, R. Inguanta, Ascorbic Acid determination using linear sweep voltammetry on flexible electrode modified with gold nanoparticles and reduced graphene oxide, in: 2020 IEEE 20th Mediterranean Electrotechnical Conference (MELECON), IEEE, Palermo, Italy, 2020, pp. 406–410, https://doi.org/10.1109/MELECON48756.2020.9140684.
[72] I. Sengupta, S. Chakraborty, M. Talukdar, S.K. Pal, S. Chakraborty, Thermal reduction of graphene oxide: how temperature influences purity, J. Mater. Res. 33 (2018) 4113–4122, https://doi.org/10.1557/jmr.2018.338.
[73] K.K.H. De Silva, H.-.H. Huang, R.K. Joshi, M. Yoshimura, Chemical reduction of graphene oxide using green reductants, Carbon N Y 119 (2017) 190–199, https://doi.org/10.1016/j.carbon.2017.04.025.
[74] C.K. Chua, M. Pumera, Chemical reduction of graphene oxide: a synthetic chemistry viewpoint, Chem. Soc. Rev. 43 (2014) 291–312, https://doi.org/10.1039/C3CS60303B.
[75] Y.C. Guan, Y.W. Fang, G.C. Lim, H.Y. Zheng, M.H. Hong, Fabrication of laser-reduced graphene oxide in liquid nitrogen environment, Sci. Rep. 6 (2016) 28913, https://doi.org/10.1038/srep28913.
[76] T.X. Tran, H. Choi, C.H. Che, J.H. Sul, I.G. Kim, S.-.M. Lee, J.-.H. Kim, J.B. In, Laser-induced reduction of graphene oxide by intensity-modulated line beam for supercapacitor applications, ACS Appl. Mater. Interfaces 10 (2018) 39777–39784, https://doi.org/10.1021/acsami.8b14678.
[77] V. Scardaci, L. Fichera, M.E. Fragalà, N. Tuccitto, G. Marletta, G. Compagnini, Reduction of graphene oxide by laser scribing in different atmospheres and application in humidity sensing, J. Nanomater. 2020 (2020) 1–7, https://doi.org/10.1155/2020/4946954.
[78] J. Liu, H. Ji, X. Lv, C. Zeng, H. Li, F. Li, B. Qu, F. Cui, Q. Zhou, Laser-induced graphene (LIG)-driven medical sensors for health monitoring and diseases diagnosis, Microchim. Acta 189 (2022) 54, https://doi.org/10.1007/s00604-021-05157-6.
[79] M. Iqra, F. Anwar, R. Jan, M.A. Mohammad, A flexible piezoresistive strain sensor based on laser scribed graphene oxide on polydimethylsiloxane, Sci. Rep. 12 (2022) 4882, https://doi.org/10.1038/s41598-022-08801-0.
[80] M.A. Zahed, S.C. Barman, P.S. Das, M. Sharifuzzaman, H.S. Yoon, S.H. Yoon, J. Y. Park, Highly flexible and conductive poly (3, 4-ethylene dioxythiophene)-poly (styrene sulfonate) anchored 3-dimensional porous graphene network-based electrochemical biosensor for glucose and pH detection in human perspiration, Biosens. Bioelectron. 160 (2020), 112220, https://doi.org/10.1016/j.bios.2020.112220.
[81] R. Barber, S. Cameron, A. Devine, A. McCombe, L. Kirsty Pourshahidi, J. Cundell, S. Roy, A. Mathur, C. Casimero, P. Papakonstantinou, J. Davis, Laser induced graphene sensors for assessing pH: application to wound management, Electrochem. Commun. 123 (2021), 106914, https://doi.org/10.1016/j.elecom.2020.106914.
[82] Z. Wan, M. Umer, M. Lobino, D. Thiel, N.-.T. Nguyen, A. Trinchi, M.J.A. Shiddiky, Y. Gao, Q. Li, Laser induced self-N-doped porous graphene as an electrochemical biosensor for femtomolar miRNA detection, Carbon N Y 163 (2020) 385–394, https://doi.org/10.1016/j.carbon.2020.03.043.
[83] D. Vanegas, L. Patiño, C. Mendez, D. Oliveira, A. Torres, C. Gomes, E. McLamore, Laser scribed graphene biosensor for detection of biogenic amines in food samples using locally sourced materials, Biosensors 8 (2018) 42, https://doi.org/10.3390/bios8020042.
[84] A.R. Cardoso, A.C. Marques, L. Santos, A.F. Carvalho, F.M. Costa, R. Martins, M. G.F. Sales, E. Fortunato, Molecularly-imprinted chloramphenicol sensor with laser-induced graphene electrodes, Biosens. Bioelectron. 124–125 (2019) 167–175, https://doi.org/10.1016/j.bios.2018.10.015.
[85] Y. Lei, A.H. Alshareef, W. Zhao, S. Inal, Laser-scribed graphene electrodes derived from lignin for biochemical sensing, ACS Appl. Nano Mater. 3 (2020) 1166–1174, https://doi.org/10.1021/acsanm.9b01795.
[86] R.R.A. Soares, R.G. Hjort, C.C. Pola, K. Parate, E.L. Reis, N.F.F. Soares, E. S. McLamore, J.C. Claussen, C.L. Gomes, Laser-induced graphene electrochemical immunosensors for rapid and label-free monitoring of *Salmonella enterica* in chicken broth, ACS Sens. 5 (2020) 1900–1911, https://doi.org/10.1021/acssensors.9b02345.
[87] T. Beduk, D. Beduk, J.I. de Oliveira Filho, F. Zihnioglu, C. Cicek, R. Sertoz, B. Arda, T. Goksel, K. Turhan, K.N. Salama, S. Timur, Rapid point-of-care COVID-19 diagnosis with a gold-nanoarchitecture-assisted laser-scribed graphene biosensor, Anal. Chem. 93 (2021) 8585–8594, https://doi.org/10.1021/acs.analchem.1c01444.
[88] S.C. Barman, Md.A. Zahed, Md. Sharifuzzaman, S.G. Ko, H. Yoon, J.S. Nah, X. Xuan, J.Y. Park, A polyallylamine anchored amine-rich laser-ablated graphene platform for facile and highly selective electrochemical IgG biomarker detection, Adv. Funct. Mater. 30 (2020), 1907297, https://doi.org/10.1002/adfm.201907297.
[89] R.M. Torrente-Rodríguez, J. Tu, Y. Yang, J. Min, M. Wang, Y. Song, Y. Yu, C. Xu, C. Ye, W.W. IsHak, W. Gao, Investigation of cortisol dynamics in human sweat using a graphene-based wireless mHealth system, Matter 2 (2020) 921–937, https://doi.org/10.1016/j.matt.2020.01.021.
[90] X. Hui, X. Xuan, J. Kim, J.Y. Park, A highly flexible and selective dopamine sensor based on Pt-Au nanoparticle-modified laser-induced graphene, Electrochim. Acta 328 (2019), 135066, https://doi.org/10.1016/j.electacta.2019.135066.
[91] Z.T. Johnson, K. Williams, B. Chen, R. Sheets, N. Jared, J. Li, E.A. Smith, J. C. Claussen, Electrochemical sensing of neonicotinoids using laser-induced graphene, ACS Sens. 6 (2021) 3063–3071, https://doi.org/10.1021/acssensors.1c01082.
[92] J. Zhu, S. Liu, Z. Hu, X. Zhang, N. Yi, K. Tang, M.G. Dexheimer, X. Lian, Q. Wang, J. Yang, J. Gray, H. Cheng, Laser-induced graphene non-enzymatic glucose sensors for on-body measurements, Biosens. Bioelectron. 193 (2021), 113606, https://doi.org/10.1016/j.bios.2021.113606.
[93] I.S. Kucherenko, D. Sanborn, B. Chen, N. Garland, M. Serhan, E. Forzani, C. Gomes, J.C. Claussen, Ion-selective sensors based on laser-induced graphene for evaluating human hydration levels using urine samples, Adv. Mater. Technol. 5 (2020), 1901037, https://doi.org/10.1002/admt.201901037.
[94] E.R. Mamleyev, S. Heissler, A. Nefedov, P.G. Weidler, N. Nordin, V. V. Kudryashov, K. Länge, N. MacKinnon, S. Sharma, Laser-induced hierarchical carbon patterns on polyimide substrates for flexible urea sensors, Npj Flex Electron. 3 (2019) 2, https://doi.org/10.1038/s41528-018-0047-8.
[95] B.A. Getachew, D.S. Bergsman, J.C. Grossman, Laser-induced graphene from polyimide and polyethersulfone precursors as a sensing electrode in anodic stripping voltammetry, ACS Appl. Mater. Interfaces 12 (2020) 48511–48517, https://doi.org/10.1021/acsami.0c11725.
[96] Y. Zhang, H. Zhu, P. Sun, C. Sun, H. Huang, S. Guan, H. Liu, H. Zhang, C. Zhang, K. Qin, Laser-induced graphene-based non-enzymatic sensor for detection of hydrogen peroxide, Electroanalysis 31 (2019) 1334–1341, https://doi.org/10.1002/elan.201900043.
[97] A. Parisi, L. Curcio, V. Rocca, S. Stivala, A.C. Cino, A.C. Busacca, G. Cipriani, D. La Cascia, V. Di Dio, R. Miceli, Photovoltaic module characteristics from CIGS solar cell modelling, in: 2013 International Conference on Renewable Energy Research and Applications (ICRERA), IEEE, Madrid, Spain, 2013, pp. 1139–1144, https://doi.org/10.1109/ICRERA.2013.6749924.

[98] A.A. Ramadan, R.D. Gould, A. Ashour, On the Van der Pauw method of resistivity measurements, Thin Solid Films 239 (1994) 272–275, https://doi.org/10.1016/0040-6090(94)90863-X.
[99] M. Battaglia, R. Inguanta, S. Piazza, C. Sunseri, Fabrication and characterization of nanostructured Ni–IrO2 electrodes for water electrolysis, Int. J. Hydrogen Energy 39 (2014) 16797–16805, https://doi.org/10.1016/j.ijhydene.2014.08.065.
[100] M.G. Insinga, R.L. Oliveri, C. Sunseri, R. Inguanta, Template electrodeposition and characterization of nanostructured Pb as a negative electrode for lead-acid battery, J. Power Sources 413 (2019) 107–116, https://doi.org/10.1016/j.jpowsour.2018.12.033.
[101] K.K. Diao, Z. Xiao, Y.Y. Zhao, Specific surface areas of porous Cu manufactured by lost carbonate sintering: measurements by quantitative stereology and cyclic voltammetry, Mater. Chem. Phys. 162 (2015) 571–579, https://doi.org/10.1016/j.matchemphys.2015.06.031.
[102] S.R. Dickman, R.H. Bray, Colorimetric determination of phosphate, Ind. Eng. Chem. Anal. Ed. 12 (1940) 665–668, https://doi.org/10.1021/ac50151a013.
[103] X. He, W. Gao, L. Xie, B. Li, Q. Zhang, S. Lei, J.M. Robinson, E.H. Hároz, S. K. Doorn, W. Wang, R. Vajtai, P.M. Ajayan, W.W. Adams, R.H. Hauge, J. Kono, Wafer-scale monodomain films of spontaneously aligned single-walled carbon nanotubes, Nat. Nanotech. 11 (2016) 633–638, https://doi.org/10.1038/nnano.2016.44.
[104] Z. Wan, S. Wang, B. Haylock, J. Kaur, P. Tanner, D. Thiel, R. Sang, I.S. Cole, X. Li, M. Lobino, Q. Li, Tuning the sub-processes in laser reduction of graphene oxide by adjusting the power and scanning speed of laser, Carbon N Y 141 (2019) 83–91, https://doi.org/10.1016/j.carbon.2018.09.030.
[105] D.H. Ha, S. Jung, H.-.J. Kim, D. Kim, W.-.J. Kim, S.N. Yi, Y. Jun, Y.J. Yun, Transition of graphene oxide-coated fiber bundles from insulator to conductor by chemical reduction, Synth. Met. 204 (2015) 90–94, https://doi.org/10.1016/j.synthmet.2015.03.018.
[106] G.K. Ramesha, S. Sampath, Electrochemical reduction of oriented graphene oxide films: an in situ Raman spectroelectrochemical study, J. Phys. Chem. C. 113 (2009) 7985–7989, https://doi.org/10.1021/jp811377n.
[107] L.M. Malard, M.A. Pimenta, G. Dresselhaus, M.S. Dresselhaus, Raman spectroscopy in graphene, Phys. Rep. 473 (2009) 51–87, https://doi.org/10.1016/j.physrep.2009.02.003.
[108] D. Yang, A. Velamakanni, G. Bozoklu, S. Park, M. Stoller, R.D. Piner, S. Stankovich, I. Jung, D.A. Field, C.A. Ventrice, R.S. Ruoff, Chemical analysis of graphene oxide films after heat and chemical treatments by X-ray photoelectron and Micro-Raman spectroscopy, Carbon 47 (2009) 145–152, https://doi.org/10.1016/j.carbon.2008.09.045.
[109] B. Cai, S. Wang, L. Huang, Y. Ning, Z. Zhang, G.-.J. Zhang, Ultrasensitive label-free detection of PNA–DNA hybridization by reduced graphene oxide field-effect transistor biosensor, ACS Nano 8 (2014) 2632–2638, https://doi.org/10.1021/nn4063424.
[110] S. Khameneh Asl, M. Namdar Habashi, A. Kianvash, A. Alipour, S. Mohini, H. Asgharzadeh, Fabrication of graphene/MoS2 nanocomposite for flexible energy storage, J. Nanostruct. 9 (2019), https://doi.org/10.22052/JNS.2019.01.004.
[111] L.G. Cançado, K. Takai, T. Enoki, M. Endo, Y.A. Kim, H. Mizusaki, A. Jorio, L. N. Coelho, R. Magalhães-Paniago, M.A. Pimenta, General equation for the determination of the crystallite size La of nanographite by Raman spectroscopy, Appl. Phys. Lett. 88 (2006), 163106, https://doi.org/10.1063/1.2196057.
[112] M.N. Costa, B. Veigas, J.M. Jacob, D.S. Santos, J. Gomes, P.V. Baptista, R. Martins, J. Inácio, E. Fortunato, A low cost, safe, disposable, rapid and self-sustainable paper-based platform for diagnostic testing: lab-on-paper, Nanotechnology 25 (2014), 094006, https://doi.org/10.1088/0957-4484/25/9/094006.
[113] C. Ma, K. Yang, L. Wang, X. Wang, Facile Synthesis of Reduced Graphene Oxide/Fe_3O_4 Nanocomposite Film, J. Appl. Biomater. Funct. Mater. 15 (2017) 1–6, https://doi.org/10.5301/jabfm.5000341.
[114] T.R. Gengenbach, G.H. Major, M.R. Linford, C.D. Easton, Practical guides for x-ray photoelectron spectroscopy (XPS): interpreting the carbon 1 s spectrum, J. Vac. Sci. Technol. A 39 (2021), 013204, https://doi.org/10.1116/6.0000682.
[115] F. Perrozzi, S. Croce, E. Treossi, V. Palermo, S. Santucci, G. Fioravanti, L. Ottaviano, Reduction dependent wetting properties of graphene oxide, Carbon 77 (2014) 473–480, https://doi.org/10.1016/j.carbon.2014.05.052.
[116] G. Jena, S. Sofia, B. Anandkumar, S.C. Vanithakumari, R.P. George, J. Philip, Graphene oxide/polyvinylpyrrolidone composite coating on 316 L SS with superior antibacterial and anti-biofouling properties, Prog. Org. Coat. 158 (2021), 106356, https://doi.org/10.1016/j.porgcoat.2021.106356.
[117] E.S. Ganya, N. Soin, S.J. Moloi, J.A. McLaughlin, W.F. Pong, S.C. Ray, Polyacrylate grafted graphene oxide nanocomposites for biomedical applications, J. Appl. Phys. 127 (2020), 054302, https://doi.org/10.1063/1.5135572.
[118] N. Sharma, V. Sharma, R. Vyas, M. Kumari, A. Kaushal, R. Gupta, S.K. Sharma, K. Sachdev, A new sustainable green protocol for production of reduced graphene oxide and its gas sensing properties, J. Sci. Adv. Mater. Devices 4 (2019) 473–482, https://doi.org/10.1016/j.jsamd.2019.07.005.
[119] A. Ganguly, S. Sharma, P. Papakonstantinou, J. Hamilton, Probing the Thermal deoxygenation of graphene oxide using high-resolution in situ X-ray-based spectroscopies, J. Phys. Chem. C. 115 (2011) 17009–17019, https://doi.org/10.1021/jp203741y.
[120] E.A. Nagul, I.D. McKelvie, P. Worsfold, S.D. Kolev, The molybdenum blue reaction for the determination of orthophosphate revisited: opening the black box, Anal. Chim. Acta 890 (2015) 60–82, https://doi.org/10.1016/j.aca.2015.07.030.
[121] T. Ueda, K. Isai, Effects of organic solvents and salts on the isomerization reaction (β→α) of Keggin-type 12-molybdophosphate anion, Anal. Sci. 29 (2013) 447–453, https://doi.org/10.2116/analsci.29.447.
[122] S. Himeno, T. Osakai, A. Saito, Voltammetric characterization of α- and β-dodecamolybdophosphates in aqueous organic solutions, BCSJ 62 (1989) 1335–1337, https://doi.org/10.1246/bcsj.62.1335.
[123] S. Himeno, A. Saito, T. Hori, Synthesis and characterization of 18-molybdopyrophosphate complex, BCSJ 63 (1990) 1602–1606, https://doi.org/10.1246/bcsj.63.1602.
[124] B.M. Jayawardane, S. Wei, I.D. McKelvie, S.D. Kolev, Microfluidic paper-based analytical device for the determination of nitrite and nitrate, Anal. Chem. 86 (2014) 7274–7279, https://doi.org/10.1021/ac5013249.
[125] J. Cui, E.E. Ogabiela, J. Hui, Y. Wang, Y. Zhang, L. Tong, J. Zhang, S.B. Adeloju, X. Zhang, Y. Wu, Electrochemical biosensor based on Pt/Au Alloy nanowire arrays for phosphate detection, J. Electrochem. Soc. 162 (2015) B62–B67, https://doi.org/10.1149/2.0701503jes.
[126] A.V. Kolliopoulos, D.K. Kampouris, C.E. Banks, Rapid and portable electrochemical quantification of phosphorus, Anal. Chem. 87 (2015) 4269–4274, https://doi.org/10.1021/ac504602a.
[127] J. Jońca, V. León Fernández, D. Thouron, A. Paulmier, M. Graco, V. Garçon, Phosphate determination in seawater: toward an autonomous electrochemical method, Talanta 87 (2011) 161–167, https://doi.org/10.1016/j.talanta.2011.09.056.
[128] J.C. Quintana, L. Idrissi, G. Palleschi, P. Albertano, A. Amine, M. El Rhazi, D. Moscone, Investigation of amperometric detection of phosphate, Talanta 63 (2004) 567–574, https://doi.org/10.1016/j.talanta.2003.11.040.
[129] L. Torrezani, A.A. Saczk, M. FirminodeOliveira, N.R. Stradiotto, L.L. Okumura, Voltammetric determination of phosphate in brazilian biodiesel using two different electrodes, Electroanalysis 23 (2011) 2456–2461, https://doi.org/10.1002/elan.201100333.